

Resonant Interaction Of Relativistic Electrons with Realistic Electromagnetic Ion-Cyclotron Wave Packets

Veronika Grach (✉ vsgrach@ipfran.ru)

Institute of Applied Physics RAS: FGBNU Federal'nyj issledovatel'skij centr Institut prikladnoj fiziki Rossijskoj akademii nauk <https://orcid.org/0000-0002-0937-5218>

Andrei Demekhov

Polar Geophysical Institute Russian Academy of Sciences: Polarnyj geofiziceskij institut Rossijskoo akademii nauk

Alexey Larchenko

Polar Geophysical Institute Russian Academy of Sciences: Polarnyj geofiziceskij institut Rossijskoo akademii nauk

Full paper

Keywords: resonant interaction, radiation belts, precipitation, relativistic electrons, EMIC waves

Posted Date: April 5th, 2021

DOI: <https://doi.org/10.21203/rs.3.rs-367172/v1>

License:  This work is licensed under a Creative Commons Attribution 4.0 International License.

[Read Full License](#)

Version of Record: A version of this preprint was published on June 21st, 2021. See the published version at <https://doi.org/10.1186/s40623-021-01453-w>.

¹ **Resonant Interaction Of Relativistic Electrons with Realistic
2 Electromagnetic Ion-Cyclotron Wave Packets**

³ Veronika S. Grach, Institute of Applied Physics of the Russian Academy of Sciences, Nizhny Novgorod, Russia, vsgrach@ipfran.ru

Andrei G. Demekhov, Institute of Applied Physics of the Russian Academy of Sciences;
Polar Geophysical Institute, Apatity, Russia, andrei@ipfran.ru

Alexey V. Larchenko, Polar Geophysical Institute, alexey.larchenko@gmail.com

5 Abstract

6 We study the influence of real structure of electromagnetic ion-cyclotron wave packets in the Earth's
7 radiation belts on precipitation of relativistic electrons. Automatic algorithm is used to distinguish
8 isolated elements (wave packets) and obtain their amplitude and frequency profiles from satellite
9 observations by Van Allen Probe B. We focus on rising-tone EMIC wave packets in the proton band,
10 with a maximum amplitude of 1.2–1.6 nT. The resonant interaction of the considered wave packets with
11 relativistic electrons 1.5–9 MeV is studied by numerical simulations. The precipitating fluxes are formed
12 as a result of both linear and nonlinear interaction; for energies 2–5 MeV precipitating fluxes are close
13 to the strong diffusion limit. The evolution of precipitating fluxes is influenced by generation of
14 higher-frequency waves at the packet trailing edge near the equator and dissipation of lower-frequency
15 waves in the He⁺ cyclotron resonance region at the leading edge. The wave packet amplitude
16 modulation leads to a significant change of precipitated particles energy spectrum during short intervals
17 of less than 1 minute. For short time intervals about 10–15 s, the approximation of each local amplitude
18 maximum of the wave packet by a Gaussian amplitude profile and a linear frequency drift gives a
19 satisfactory description of the resonant interaction.

20 Keywords

21 resonant interaction; radiation belts; precipitation; relativistic electrons; EMIC waves

22 Introduction

23 The dynamics of Earth radiation belts has been studied experimentally and theoretically for many years
24 (Kennel and Petschek 1966; Tverskoy 1969; Lyons and Thorne 1973; Bespalov and Trakhtengerts 1986;
25 Trakhtengerts and Rycroft 2000; Millan and Thorne 2007; Morley et al. 2010; Li and Hudson 2019). The
26 Van Allen Probes, working from 2012 to 2019, have provided a variety of data and lots of opportunities
27 for analysis and modeling (Mauk et al. 2013).

28 Precipitation of relativistic electrons is one of the most interesting phenomena of radiation belts physics.
29 The resonant interaction of relativistic electrons with electromagnetic ion-cyclotron (EMIC) waves is
30 believed to be one of the main causes of this precipitation (Thorne and Kennel 1971).

31 First studies of resonant interaction of relativistic electrons with EMIC waves have been within the
32 framework of the quasi-linear theory (Summers and Thorne 2003; Jordanova et al. 2008; Shprits et al.
33 2009). However, observation of quasi-monochromatic wave packets with large amplitudes from 1 to 14 nT
34 (Kangas et al. 1998; Demekhov 2007; Engebretson et al. 2007; Engebretson et al. 2008; Pickett et al. 2010;
35 Nakamura et al. 2019) inspired analysis of possible nonlinear resonant interaction and its influence on
36 precipitation (Albert and Bortnik 2009; Artemyev et al. 2015; Omura and Zhao 2012, 2013; Kubota and
37 Omura 2017; Grach and Demekhov 2018a,b, 2020a). Also, there are observations of rapid loss of the
38 outer radiation belt (Morley et al. 2010; Nakamura et al. 2019), which is too fast to be explained by
39 quasi-linear diffusion rates, and thus requires nonlinear analysis.

40 Nonlinear theory of wave-particle interaction has been studied extensively for various wave modes
41 (Karpman et al. 1974; Albert 1993, 2000; Albert and Bortnik 2009; Artemyev et al. 2015; Artemyev
42 et al. 2017). The features of various interaction regimes were described analytically, including trapping
43 by the wave field (Karpman et al. 1974; Albert 1993; Demekhov et al. 2006, 2009; Artemyev et al. 2015),
44 phase bunching or nonlinear scattering (Albert 1993, 2000; Artemyev et al. 2017) and force bunching
45 (Lundin and Shkliar 1977).

46 Wave-particle interaction with finite wave packets with various amplitude and frequency profiles has been
47 studied mostly by test particle simulations (Tao et al. 2012; Zhang et al. 2018; Omura and Zhao 2012,
48 2013; Kubota and Omura 2017; Grach and Demekhov 2018a,b, 2020a). Regimes like directed scattering
49 (Kubota and Omura 2017; Grach and Demekhov 2020a,b) or nonlinear shift of the resonance point (Grach
50 and Demekhov 2020a) were revealed and analyzed.

51 For whistler mode waves, it was shown that for realistic wave packets, nonlinear effects are much weaker
52 than for single-frequency waves with a constant wave amplitude, because of the effects of amplitude
53 modulation and short packet length (Tao et al. 2012; Zhang et al. 2018).

54 For EMIC waves, test particle simulations showed that resonant interaction of relativistic electrons with
55 rising-tone EMIC wave packets can be very effective (Omura and Zhao 2012, 2013; Kubota and Omura
56 2017; Grach and Demekhov 2018b, 2020a). Precipitation flux in this case is heavily influenced and
57 increased by nonlinear effects (Grach and Demekhov 2020a).

58 Test particle simulations for resonant interaction with EMIC waves use model wave packets with main
59 parameters based on observations. In particular, our previous paper (Grach and Demekhov 2020a) used

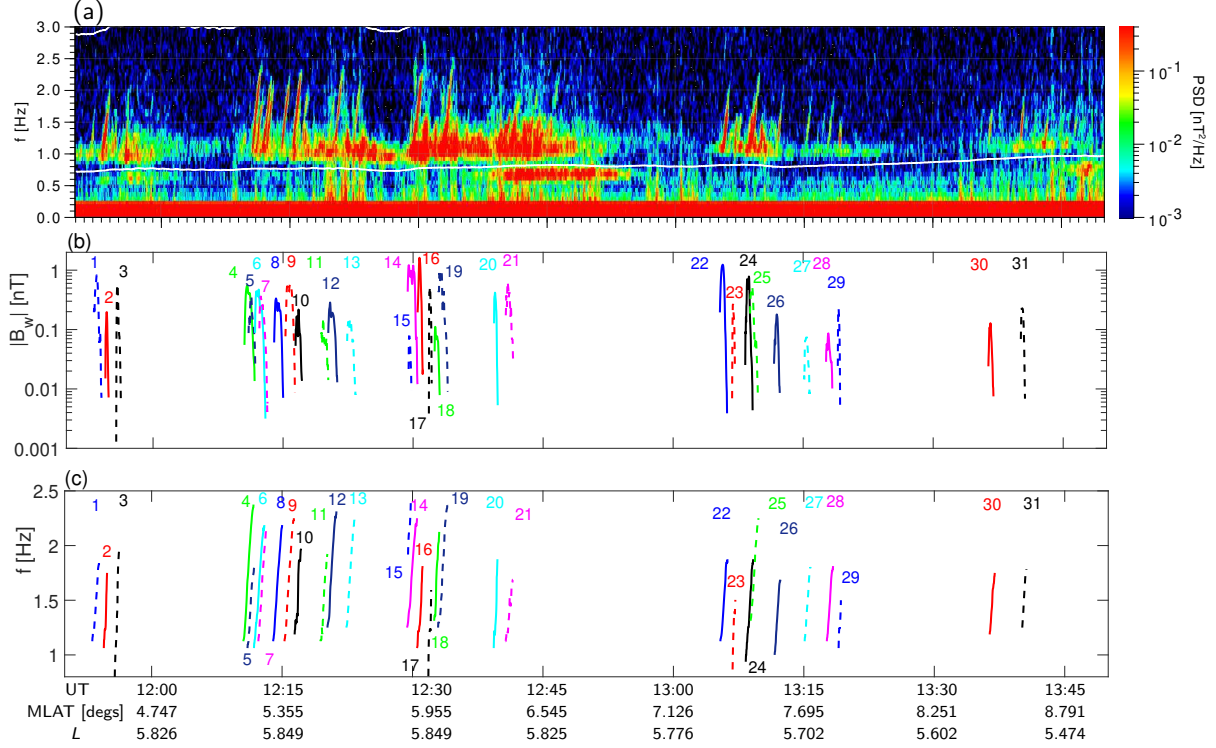


Figure 1. (a) Dynamic spectrum from 11:50 to 13:50 UT 2017-09-14; (b) obtained wave amplitude profile of discrete elements and (c) obtained wave frequency profile of discrete elements. The elements are numbered in chronological order, corresponding to the first data point.

model wave packets with linear frequency profile and two amplitude profiles, flat and Gaussian-shaped.
 (Kubota and Omura 2017) used a more complicated structure with several subpackets but without direct correspondence to observational data.
 Fine structure of a wave packet can play important role in the resonant interaction, both in linear and nonlinear regimes. In this paper we study packets directly corresponding to satellite observations from 14 September 2017, made by Van Allen Probe B.

Wave Packet Modeling

Data processing

We choose the event of 14 September 2017, the EMIC dynamic spectrum is shown in Figure 1a. We focus on rising-tone EMIC wave packets in proton band.
 Discrete elements were identified by using an algorithm developed by (Larchenko et al. 2019). The parameters of the algorithm were chosen so as to ensure 90 % of the wave packet energy to be confined in the detected elements. The instant amplitude and frequency of the wave packet were obtained by

Table 1. Parameters for wave packet modeling.

No.	λ_S	L	N_{eL} , cm $^{-3}$	N_{He} , %	N_O , %	z_{start}/z_d
14	5.9°	5.47	33.3	5.5	5.5	$-0.03R_E/0.51Z_X$
22	7.4°	5.39	33.5	7	7	$-0.1R_E/0.75Z_X$

⁷³ integration over the element area at any time.

⁷⁴ We distinguished 31 isolated element (wave packet) and obtained their amplitude and frequency profiles
⁷⁵ (see Figure 1b,c). The maximum wave amplitude is about 1.2–1.6 nT. Some of these elements can
⁷⁶ be considered isolated, some are overlapping in time and space. We divide 31 element in 12 groups,
⁷⁷ containing from 1 to 4 elements each and with duration from 40 to 250 s. We assume that each group
⁷⁸ corresponds to a fixed satellite location, and the plasma parameters stay constant during the generation,
⁷⁹ propagation and dissipation of elements in the group.

⁸⁰ We assume that EMIC wave packets are generated near the equator, propagate along the geomagnetic
⁸¹ field line and then dissipate in the He $^+$ cyclotron resonance region located father from the equator than
⁸² the spacecraft. We use the dipole geomagnetic field model and obtain McIlwain parameter L using the
⁸³ satellite geomagnetic latitude λ_S and the measured geomagnetic field B_0 . The gyrotropic model of the
⁸⁴ field-aligned profile of plasma density is used ($N_e \propto B_0$), and the measured local density is averaged over
⁸⁵ the group duration.

⁸⁶ We study the wave-particle interaction with a single packet. For this study, we choose elements 14 and
⁸⁷ 22, which amplitudes are high enough for nonlinear interaction. The element 14 is overlapped with
⁸⁸ elements 15 and 16, but we neglect element 15 because of its small amplitude (the ratio of amplitudes
⁸⁹ $B_{w14}/B_{w15} = 10 \div 100$) and we will focus our study of element 14 to times before element 16 is generated.

⁹⁰ The values of plasma parameters L, λ_S, N_e , corresponding to elements 14 and 22, are shown in Table 1.
⁹¹ Hereafter, the subscripts L and S denote the values at the equator and at the spacecraft location,
⁹² respectively. The other parameters, shown in Table 1, are discussed below.

93 **Modeling of Wave Packet Propagation**

94 **Propagation Properties** We model the wave packet propagation in the geometrical-optics approx-
95 imation, i.e., assume that each point propagates with a local group velocity V_{gr} and has its own frequency
96 that does not vary during the propagation. The amplitude variation is discussed below.

97 We use the following additional simplifying assumptions for the wave generation and dissipation. (1)

98 Each point of the packet is generated at a single point $z_{\text{start}} < 0$ near the equator and then propagates
99 with increasing coordinate z along the geomagnetic field line ($z = 0$ corresponds to the equator). (2) The
100 wave packet dissipates when it approaches the He^+ cutoff $z = Z_X(f)$ as detailed below. (3) We restrict
101 the simulation parameters in such a way that the wave packet is not broken, i.e., the trajectories of its
102 points do not intersect.

103 The propagation is modeled by using the following algorithm. For each wave packet, we have the frequency
104 profile $f_j(T_j)$ at the spacecraft location, where $j = 1 \dots M$, and $j = 1, M$ correspond to the leading and
105 trailing edges of the packet, respectively. For each data point we calculate the propagation “backwards”
106 to z_{start} and obtain profile $f_j(t_j)$, where t_j is the generation time at z_{start} . Then for each point we
107 calculate the propagation “forward” until the packet dissipates near cutoff location $Z_X(f_j) \equiv Z_X$.

108 For this approach to work we have to place some restrictions on plasma composition, i.e. the He^+ density,
109 to ensure the absence of wave packet breaking during the propagation. The dependence of group velocity
110 V_{gr} on f/f_{He^+} (f_{He^+} — local helium gyrofrequency) is non monotonic: V_{gr} decreases with f/f_{He^+} far from
111 cutoff frequency and increases with f/f_{He^+} close to it. For a wave packet with strong enough negative
112 frequency gradient (rising tone) the intersection of the trajectories (i.e, the amplitude profile breaking)
113 is possible for the points with higher frequencies (trailing edge of the wave packet) when we calculate
114 the propagation “backward” from the satellite to the equator. This happens if cutoff locations are too
115 far away from the satellite location (N_{He^+} too low), thus decreasing of V_{gr} with f/f_{He^+} is too abrupt.

116 On the other hand, when a wave packet with rising tone propagates “forward” away from the equator
117 and nears the cutoff locations, the trajectories of the points with lower frequencies (leading edge of the
118 wave packet) intersect, which leads to the wave packet distortion. This distortion cannot be correctly
119 described by geometrical optics, so we need to gradually dissipate the wave packet, starting from the
120 leading edge, before this distortion happens. For the model wave packet to correspond to satellite data,
121 this dissipation should begin after the satellite location, which means that cutoff locations shouldn’t be

122 too close to the satellite location (N_{He^+} can't be too high). Thus, the value of N_{He^+} should be high
 123 enough that "backward" propagation from the satellite to the equator is possible without distortion and
 124 at the same time N_{He^+} should be low enough for the correct "forward" propagation from the equator
 125 to the satellite. The values for two considered wave packets are shown in Table 1. We also assume
 126 $N_{\text{O}^+} = N_{\text{He}^+}$.

127 Due to the properties of wave packet propagation, discussed above, "forward" propagation to the equator
 128 (from z_{start} to $z = 0$) without distortion is possible only in a small region. The values of z_{start} (chosen as
 129 the maximum possible $|z_{\text{start}}|$) are also shown in Table 1 (hereafter, R_E denotes the Earth radius).

130 **Amplitude and Phase of the Wave Packet** We assume that there is a small region Δz_{gen}
 131 where the wave packet is generated (its energy increases), the small region Δz_{damp} where wave packet
 132 dissipates (its energy decreases, after the satellite) and in between for each point of the packet its energy
 133 $\mathcal{E} \propto B_w^2 V_{\text{gr}} / (8\pi)$ remains constant and corresponds to the satellite data. We choose the following model:

$$\mathcal{E}(f_j) = \begin{cases} \mathcal{E}_{S,j} \delta_{\text{gen}} \exp[\gamma_{\text{gen},j}(z - z_{\text{start}})], & z_{\text{start}} \leq z \leq z_{c,j}; \\ \mathcal{E}_{S,j}, & z_{c,j} < z \leq z_{\text{damp},j}; \\ \mathcal{E}_{S,j} \exp[-\gamma_{\text{damp},j}(z - z_{\text{damp},j})^2], & z_{\text{damp},j} < z < \min\{0.99Z_{X,j}, z_{\text{cr},j}\}. \end{cases} \quad (1)$$

134 Here $j = 1 \dots M$, $z_{\text{cr},j}$ is the location of possible trajectory intersection, $\delta_{\text{gen}} = 1/50$, $\gamma_{\text{gen},j} = -\ln \delta_{\text{gen}} / (z_{c,j} -$
 135 $z_{\text{start}})$, $z_{c,j} = z_{\text{start}} + \Delta z_{\text{gen},j}$, $\gamma_{\text{damp},j} = 5 \ln 10 / (Z_{X,j} - z_{\text{damp},j})^2$.

136 We choose $\Delta z_{\text{gen},j} = 0.1Z_{X,j}$, thus the generation region takes up to 10 % of the area of wave packet
 137 existence. The relation between z_{damp} and Z_X is chosen empirically for each wave packet, to ensure that
 138 wave amplitude is small enough at the dissipation point. The values of z_{damp} are shown in Table 1.

139 We also calculate the change in the wave phase for the leading and trailing edges of the packet:

$$\vartheta_j = \int k_j dz - \int \omega_j dt = \frac{\omega_j}{c} \int n_j dz - \omega_j t. \quad (2)$$

140 Here $\omega_j = 2\pi f_j$, k_j and n_j are wave number and refractive index for the frequency f_j , respectively. We
 141 set $\vartheta_j = 0$ at $z = z_{\text{start}}$ for any j .

142 While the packet is generated, the trailing edge of the packet is located at z_{start} and so the phase of the
 143 trailing edge $\vartheta_{\text{te}} = 0$. Once the generation is finished, $\vartheta_{\text{te}} = \vartheta_M$ and changes smoothly. On the contrary,
 144 the phase of the leading edge changes smoothly at first, while $\vartheta_{\text{le}} = \vartheta_1$, then, once the packet starts to
 145 dissipate, $\vartheta_{\text{le}} = \vartheta_j$, where j increases (the leading edge frequency increases until the packet dissipates

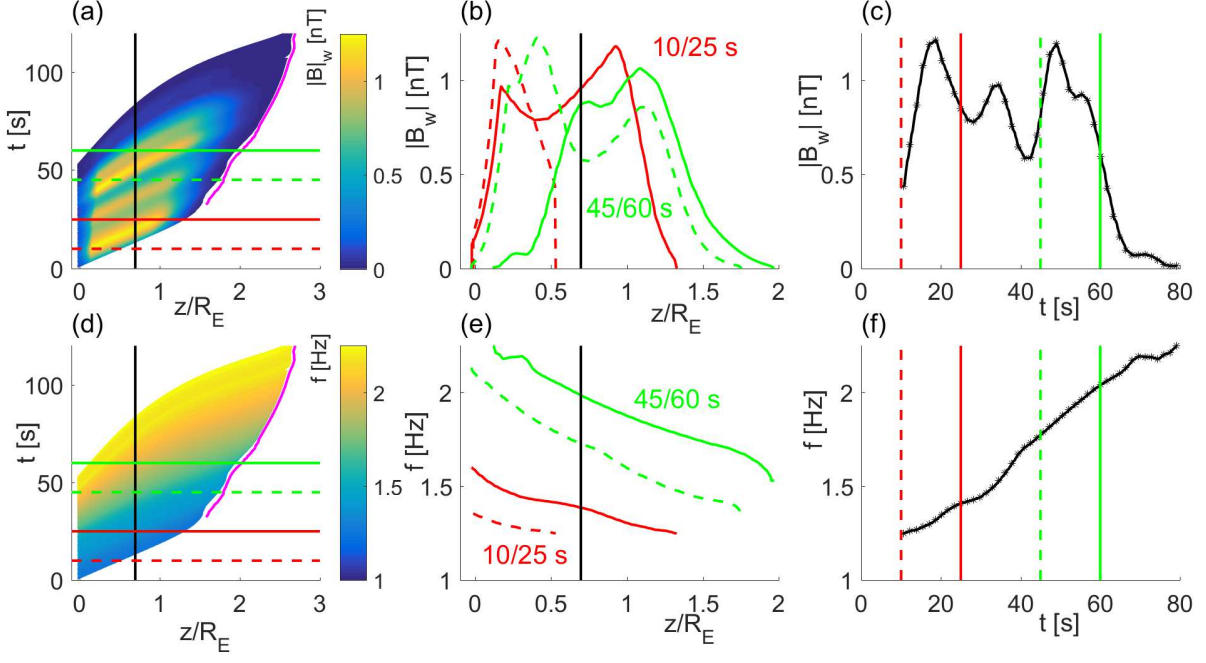


Figure 2. Wave packet propagation for element 14: amplitude (a–c) and frequency (d–f) profiles. Panels b and e show spatial profiles at $t = 10$ s (dashed red line), 25 s (solid red line), 45 s (dashed green line) and 60 s (solid green line). Panels c and f show temporal profiles at the satellite location $z = z_S$ (black solid line), black markers represent the data from Figure 1. Times 10; 25; 45 and 60 s are shown in panels a, d by horizontal lines and in panels c, f by vertical lines. Location $z = z_S$ is shown in panels a, d, b, e by vertical lines.

146 completely).

147 The results of wave packets modeling are shown in Figures 2 and 3. Hereafter time t starts at the
148 generation moment of the leading edge of the packet.

149 As one can see from Figures 2,3, all the frequencies which can be seen in satellite data do not exist at the
150 same time. By the time the wave with the highest frequency in the packet (trailing edge) is generated, the
151 waves with lowest frequencies (leading edge) have been already dissipated at the He^+ resonance. That
152 means that any space profile will contain only part of the frequency spectrum.

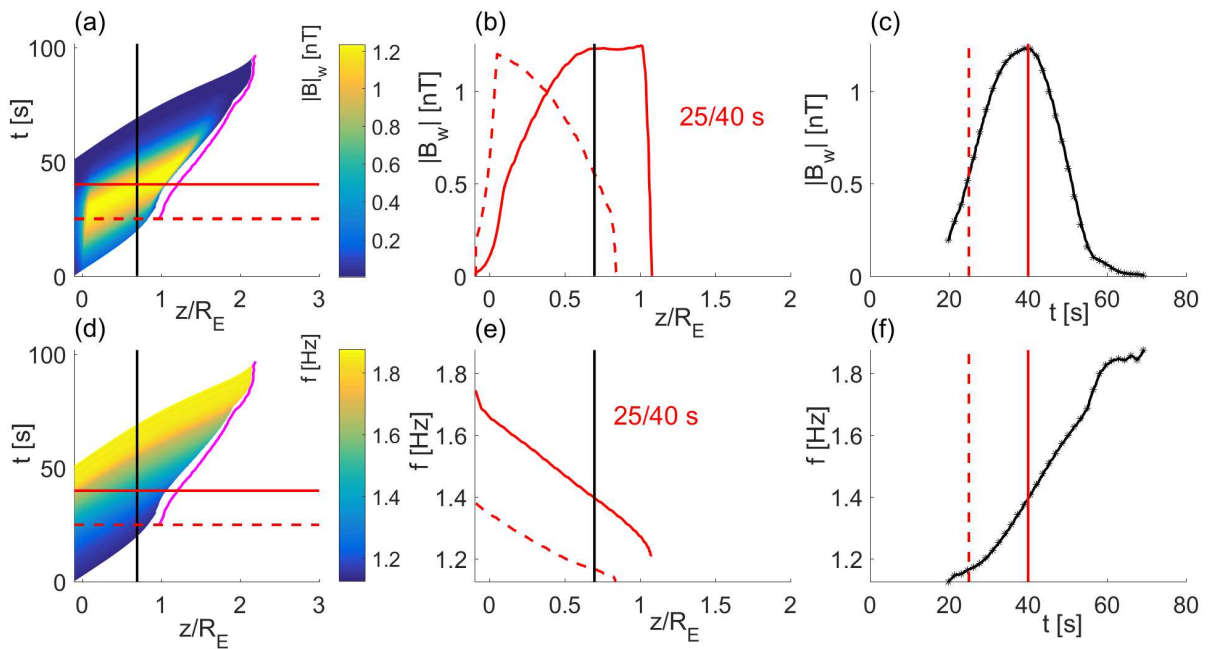


Figure 3. Wave packet propagation for element 22: amplitude (a–c) and frequency (d–f) profiles. Panels b and e show spatial profiles at $t = 25$ s (dashed red line) and 40 s (solid red line). Panels c and f show temporal profiles at the satellite location $z = z_S$ (black solid line), black markers represent the data from Figure 1. Times 25 and 40 s are shown in panels a, d by horizontal lines and in panels c, f by vertical lines. Location $z = z_S$ is shown in panels a, d, b, e by vertical lines.

153 **Wave-Particle Interaction. Theory**

154 **Basic equations**

155 The resonant interaction with parallel-propagating EMIC waves is possible only for relativistic electrons
 156 and at the anomalous cyclotron resonance. The resonance condition is written as follows:

$$\Delta = \omega - kv_{||} + \Omega_c/\gamma = 0, \quad (3)$$

157 where ω and k are wave frequency and number, respectively, $v_{||}$ is field-aligned velocity, $\Omega_c = eB_0/mc$,
 158 B_0 is geomagnetic field, $e > 0$ is elementary charge, $\gamma = \sqrt{1 + [p/(mc)]^2}$, m and p are the electron rest
 159 mass and momentum, respectively.

160 We use the same equations of motion for test electrons interacting with EMIC waves as (Grach and
 161 Demekhov 2020a):

$$\frac{dW}{dt} = -ev_{\perp}|E_w|\sin\Psi; \quad (4)$$

$$\frac{dI_{\perp}}{dt} = -\frac{2e}{mB_0}p_{\perp}(1 - n_{||}\beta_{||})|E_w|\sin\Psi; \quad (5)$$

$$\frac{d\Psi}{dt} = -\Delta - \frac{e}{p_{\perp}}(1 - n_{||}\beta_{||})|E_w|\cos\Psi; \quad (6)$$

$$\frac{dz}{dt} = \frac{p_{||}}{m\gamma}. \quad (7)$$

162 Here the subscripts $||$ and \perp denote projections to the parallel and transverse directions with respect
 163 to \mathbf{B}_0 , respectively, E_w is slowly changing wave electric field amplitude, $n_{||} = kc/\omega$, $\Psi = \vartheta - \varphi$, φ
 164 is the gyrophase in the geomagnetic field \mathbf{B}_0 , ϑ is the wave phase, $\beta_{||} = v_{||}/c$, $W = (\gamma - 1)mc^2$ and
 165 $I_{\perp} = p_{\perp}^2/(mB_0)$ are the electron kinetic energy and the first adiabatic invariant respectively, and z is
 166 coordinate along the geomagnetic field with $z = 0$ corresponding to the equator. In the right-hand side
 167 of equation (6) the first term represents inertial, or kinematic bunching, while the second one represents
 168 the direct influence of Lorentz force on the particle phase (force bunching).

169 For EMIC waves $\omega \ll \Omega_c$, and thus the resonant interaction is possible only for $k_{||}v_{||} > 0$ and the change in
 170 electron energy W will be insignificant: $\gamma \approx \text{const}$ (Bespalov and Trakhtengerts 1986; Albert and Bortnik
 171 2009). The interaction result is described by the change in the adiabatic invariant I_{\perp} or equatorial pitch
 172 angle Θ_L , $\mu = \sin^2\Theta_L = (p_{\perp}^2/p^2)(B_L/B_0)$.

176 **Summary of earlier analytical results**

177 For the reader's convenience, we briefly summarize earlier results of various authors (Karpman et al.
 178 1974; Albert 1993, 2000; Albert and Bortnik 2009; Kubota and Omura 2017; Grach and Demekhov
 179 2018a, 2020a).

180 Particle behavior during the interaction (interaction regime) is determined by the inhomogeneity param-
 181 eter $\mathcal{R} = \sigma_R R$ (Karpman et al. 1974; Albert 1993, 2000; Albert and Bortnik 2009; Kubota and Omura
 182 2017; Grach and Demekhov 2018a), where $\sigma_R = \pm 1$ determines the effective inhomogeneity sign, and

$$R = \frac{|d\Delta/dt|}{\Omega_{tr}^2}. \quad (8)$$

183 Here Ω_{tr}^2 is frequency of electron oscillations in the wave field near the effective potential minimum (Grach
 184 and Demekhov 2018a; Demekhov et al. 2006). Under real conditions, the parameter R changes both in
 185 time and in space. These changes are associated both with medium inhomogeneity (including changes
 186 in the wave packet frequency and amplitude) and nonlinear changes in the particle parameters during
 187 the interaction. However, the main features of the particle motion can be categorized based on the R
 188 values calculated at the resonance point in the linear approximation. For $R > 1$, the trajectories of all
 189 particles on the phase plane are open (all particles are untrapped), and for $R < 1$ there is a minimum
 190 of the wave effective potential, i.e. particle trapping by the wave field is possible. The phase trajectories
 191 of the trapped particles are closed. For resonant interaction of electrons with EMIC wave packet, which
 192 is generated near the equator and propagates away from it, the effective inhomogeneity is negative.

193 Hereafter, we assume $\sigma_R = -1$.

194 The case of $R \gg 1$ corresponds to the linear regime. In this case the change in particle equatorial pitch
 195 angle depends on initial phase. For an ensemble of particles with initial phases uniformly distributed in
 196 $[0, 2\pi)$ pitch angle diffusion takes place (Albert 2000; Albert and Bortnik 2009; Grach and Demekhov
 197 2018a, 2020a):

$$\langle \Delta\mu \rangle^{\text{lin}} = 0; \quad (9)$$

$$\sqrt{\langle (\Delta\mu^{\text{lin}} - \langle \Delta\mu \rangle^{\text{lin}})^2 \rangle} = \sigma_\mu^{\text{lin}} > 0. \quad (10)$$

199 Hereafter, angle brackets denote phase averaging. The root mean square deviation σ_μ determines the
 200 diffusion coefficients in the linear regime.

201 For $R \leq 1$, the resonant interaction is nonlinear, which leads to drift in pitch angles for both trapped and
 202 untrapped particles. For relativistic electrons interacting with EMIC waves, propagating away from the

203 equator, trapping can lead to a significant decrease in pitch angle (Albert and Bortnik 2009; Kubota and
 204 Omura 2017; Grach and Demekhov 2018a, 2020a). For most of the untrapped particles, phase bunching
 205 without trapping or nonlinear scattering takes place (Albert 1993, 2000; Artemyev et al. 2017), which
 206 leads to pitch angle increase (Albert and Bortnik 2009; Grach and Demekhov 2018b, 2020a). When $R < 1$
 207 is not too small, directed scattering, which leads to a significant pitch angle decrease, is possible for a
 208 small group of untrapped particles (Kubota and Omura 2017; Grach and Demekhov 2018a, 2020a).
 209 Nonlinear effects can also take place for not too high $R \geq 1$. If the wave amplitude is high enough, then
 210 the resonance point is shifted during the interaction. It leads to particles with the same initial pitch
 211 angle but different initial phases having different resonance points, and, consequently, different values
 212 of R . When dependence $R(\mu)$ is significant, that causes drift in μ ($\langle \Delta\mu \rangle \neq 0$) (Grach and Demekhov
 213 2020a). Force bunching (the Lorentz force term in Eq. (6) for the particle phase, which is neglected
 214 in linear approximation) becomes significant for particles with low Θ_L . It was shown analytically by
 215 (Lundin and Shkliar 1977) that force bunching leads to systematic increase in electron pitch angle for
 216 resonance electrons with low transverse velocities in the field of a whistler mode parallel propagating wave.
 217 Lately, numerical simulations showed similar results for electrons interacting with EMIC waves (Grach
 218 and Demekhov 2020a), right-hand extraordinary mode (Grach and Demekhov 2020b), and whistler waves
 219 (Kitahara and Katoh 2019). It was showed in (Grach and Demekhov 2020a) that force bunching can
 220 completely block precipitation from low pitch angles close to the loss cone.

221 **Wave-Particle Interaction. Numerical Calculations**

222 The system (4)–(7) was solved numerically by Bogacki-Shampine variant of the Runge-Kutta method.
 223 For every energy calculations were done for 82 values of equatorial pitch angle (range 4° – 85° , step of 1
 224 degree) and 360 values of the initial phase (uniformly in $[0, 2\pi]$). Thus, for every energy, the trajectories of
 225 29520 particles were calculated. We assume particle energies $1 \text{ MeV} \leq W_0 \leq 10 \text{ MeV}$. At the beginning of
 226 simulation $t = t_{\text{begin}}$ all particles are placed at the point $z = -0.1R_E$ with positive longitudinal velocities.
 227 As is shown below, this is insignificant for the results, since the particles are spread over the field line in
 228 4–8 bounces. If a particle is in the loss cone after leaving the packet ($\Theta_L < \Theta_{Lc}$), then the simulation
 229 for this particle is stopped. For both considered sets of plasma parameters, the equatorial pitch angle,
 230 corresponding to the loss cone, $\Theta_{Lc} \approx 3.4^\circ$.

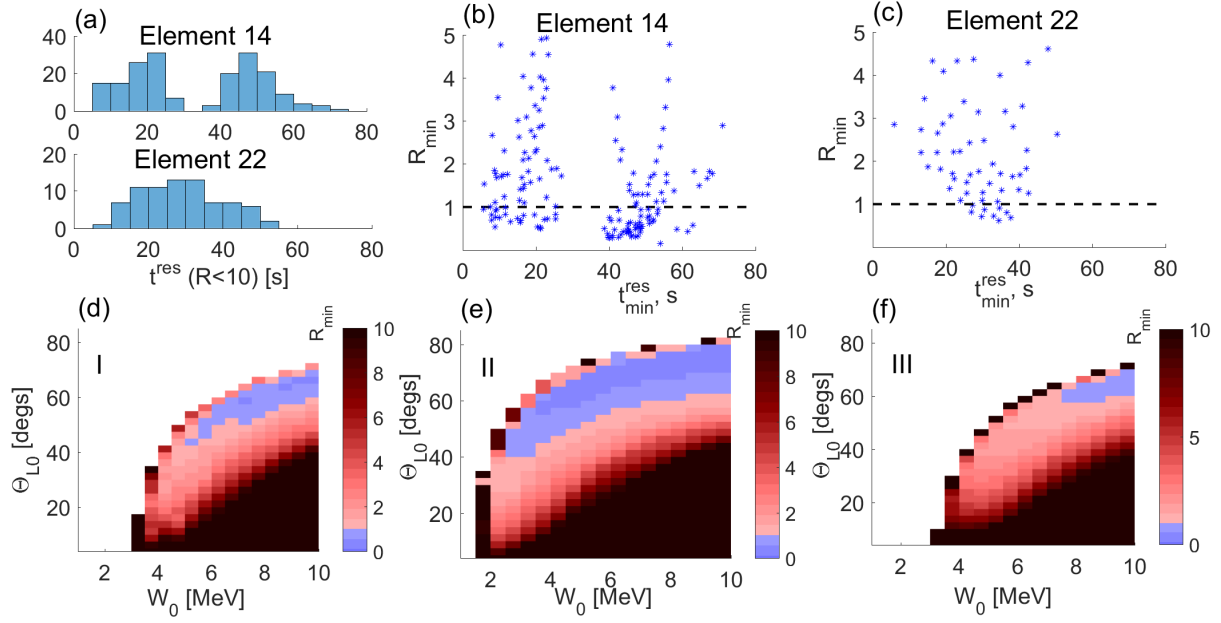


Figure 4. Resonance conditions. Distribution of resonance points with $R < 10$ over time (a) and dependencies of $R_{\min} \leq 5$ on time (b,c) for the whole packet. Dependencies $R_{\min}(\Theta_{L0}, W_0)$ for the chosen time intervals: element 14, 10–25 s (case I, d), element 14, 45–60 s (case II, e), element 22, 25–40 s (case III, f). On the bottom panels the R_{\min} scale is limited by $R = 10$.

231 Change in phase Ψ is calculated according to (6) when a particle is inside the wave packet. The phase
 232 on the particle next entrance in the packet is calculated taking into account the increments in particle
 233 gyrophase φ and in the wave phase ϑ for the packet edges (ϑ_{le} and ϑ_{te} , see (2)).

234 Preliminary Analysis of Resonance Conditions

235 Our simulation model, based on equations (4)–(7), doesn't take into account the effect of magnetic drift
 236 on the electron distribution function in a given flux tube. To justify this approximation, we must limit our
 237 simulation to times which don't exceed drift times across the wave packet. These times are significantly
 238 shorter than 100–120 s of wave packets existence (specific values are discussed below). To determine
 239 simulation time and range of test particle energies, we first analyze resonant conditions for the considered
 240 wave packets and the behavior of inhomogeneity parameter R unperturbed values.

241 If the frequency range of the wave packet remains constant during the simulation, we can analyze resonant
 242 conditions for the single pass through the wave packet near the equator and then predict their behavior
 243 during wave packet propagation (Grach and Demekhov 2018a, 2020a). With lower-frequency waves
 244 dissipating and higher-frequency waves generating during possible simulation time (see bottom panels of
 245 Figures 2 and 3), we have to analyze resonance points and R values at these points for the whole time
 246 when the wave packet exists.

247 In Figure 4a the distribution of resonance points with $R < 10$ over time is shown for both wave packets.

248 In Figure 4b and c, we show time dependencies of minimum R values over the trajectory (for $R_{\min} \leq 5$).

249 Based on these calculations and several test simulations we choose three cases for our further simulations:

250 (I) element 14, time interval 10–25 s; (II) element 14, time interval 45–60 s; (III) element 22, time interval

251 25–40 s. Dependencies of $R_{\min}(\Theta_{L0}, W_0)$ for these three cases are shown at bottom panels of Figure 4.

252 These intervals correspond to the most effective wave-particle interaction and represent all the possible

253 interaction regimes. Note that taking into account wave packet dissipation in the He^+ cyclotron resonance

254 region allowed us to use longer simulation time than in (Grach and Demekhov 2020a) (15 s instead of

255 6.5 s).

256 These time intervals are shown in Figures 2 and 3, as well as spatial profiles of wave amplitude and

257 frequency at the start and end of the intervals (hereafter, t_{begin} and t_{end} , respectively). As one can

258 see from the Figures, Case I (element 14, time interval 10–25 s) corresponds to the biggest changes in

259 the packet length during the interaction interval. We can also see that in Case I there is an active

260 generation of higher-frequency waves at the trailing edge during the simulation time but dissipation of

261 lower-frequency waves at the leading edge doesn't take place. Case II (element 14, time interval 45–60 s)

262 corresponds to the widest frequency range (1.4–2.35 Hz) and to the longest wave packet spatial structure

263 (close to $2R_E$). Generation of the packet is mostly finished by the beginning of Case II, but dissipation

264 of lower-frequency waves has started. Case III (element 22, time interval 25–40 s) corresponds to the

265 strongest increase in frequency; both generation and dissipation take place during the simulation time.

266 The highest frequencies in Case II result in the lowest resonant energies (see Figure 4e). We also can

267 see that Case II has the largest range of resonant pitch angles and the widest area of possible nonlinear

268 interaction (corresponding to lower R values). It is noteworthy that the zone of resonant interaction is

269 determined by the effective wave packet length for the considered packets, since the zone determined by

270 the phase mismatch is wider.

271 The calculations were done in the following energy ranges: 3.5 \div 8.0 MeV for Case I, 1.5 \div 5.5 MeV for

272 Case II and 3.5 \div 9.0 MeV for Case III, with steps of 0.5 MeV. Here the lower limit corresponds to the

273 lowest energy for which the range of resonant pitch angles exceeds 20° , the upper limit is chosen based

274 on test estimates on precipitation flux (see below).

275 For particles with maximum considered energy 9 MeV the chosen simulation duration of 15 s corresponds

276 to the drift time across an arc of 5° , which seems reasonable transverse size for an EMIC wave packet.
277 For longer time intervals, drift effects have to be taken into account. The chosen time interval 15 s
278 corresponds to 25–50 bounce periods.

279 **Interaction regimes**

280 First, we study which interaction regimes are possible for the considered wave packets and particle
281 ensemble, and how their features depend on particle parameters and wave packet evolution.

282 In this section we analyze the interaction regimes based on phase averaged change in $\mu = \sin^2 \Theta_L$ after
283 a single pass through wave packet. In Figure 5, we plot $\langle \Delta\mu \rangle(\Theta_L)$ and $\sigma_\mu(\Theta_L)$ for two moments during
284 the simulation, where Θ_L is the equatorial pitch angle before the pass through the packet.

285 The dependencies $\langle \Delta\mu \rangle(\Theta_L, W_0)$, $\sigma_\mu(\Theta_L, W_0)$ are similar for all three cases and are also in agreement
286 with previous results for model wave packets with Gaussian amplitude profile (Grach and Demekhov
287 2020a).

288 For lower energies (close to the lower limit of the resonant range, top row in Figure 5) small positive
289 maximum of $\langle \Delta\mu \rangle$ at smaller Θ_L is related to force bunching, with small influence of nonlinear shift of
290 the resonance point. The negative minimum of $\langle \Delta\mu \rangle$ at higher Θ_L is also caused by nonlinear shift of the
291 resonance point (trapping by the wave field is not possible at these energies, see Figure 4). For higher
292 energies (close to the upper limit of the resonant range, bottom row in Figure 5), positive maximum of
293 $\langle \Delta\mu \rangle$ is located at intermediate Θ_L and caused by a nonlinear shift of the resonance point with a small
294 influence of phase bunching. A strong negative minimum near the upper limit of resonant range of Θ_L is
295 related to the particle trapping by the wave field. The nonlinear effects are the strongest ($|\langle \Delta\mu \rangle| \geq \sigma_\mu$)
296 for lower energies and low pitch angles close to the loss cone and for trapping (Case II, higher energies).

297 For higher energies and relatively wide range of $\Theta_L < 25^\circ\text{--}40^\circ$, the interaction is linear ($\langle \Delta\mu \rangle(\Theta_L) \approx 0$)
298 with small rms deviation σ_μ (and, consequently, small diffusion coefficients).

299 With increasing energies (from top row to bottom in Figure 5), the extrema of $\langle \Delta\mu \rangle(\Theta_L)$ are shifted to
300 the higher values of Θ_L .

301 The influence of complicated packet structure (in comparison with simpler models (Grach and Demekhov
302 2018b, 2020a)) can be seen in the temporal dynamics of the dependencies $\langle \Delta\mu \rangle(\Theta_L), \sigma_\mu(\Theta_L)$. For
303 dependencies $\langle \Delta\mu \rangle(\Theta_L)$, only Case II shows roughly the same temporal dynamics as the model wave
304 packets, considered in (Grach and Demekhov 2018b, 2020a): $|\langle \Delta\mu \rangle(\Theta_L)|$ decreases with time, and the

305 extrema of $\langle \Delta\mu \rangle(\Theta_L)$ are shifted to the lower values of Θ_L . For Cases I and III, $|\langle \Delta\mu \rangle(\Theta_L)|$ can either
306 increase or decrease and the extrema of $\langle \Delta\mu \rangle(\Theta_L)$ are shifted to the higher values of Θ_L .

307 This dynamics is explained as follows. For electrons with lower energies and/or higher pitch angles
308 (corresponding to extrema in $\langle \Delta\mu \rangle(\Theta_L)$), the resonance points are located closer to the trailing edge.
309 Therefore, the resonant interaction with these particles will be strongly influenced by generation of
310 higher-frequency waves at the packet trailing edge near the equator. For Case II, the generation of
311 higher-frequency waves during the simulation time is not significant (see Figure 2): generation stops
312 in the middle of the simulation, the increase of trailing edge frequency is small and the amplitudes of
313 the generated waves are low. Thus, evolution of $\langle \Delta\mu \rangle(\Theta_L)$ in Case II is caused mostly by wave packet
314 propagation, like in (Grach and Demekhov 2020a). On the contrary, for Cases I and III, generation of
315 higher-frequency waves at the equator during the simulation time plays an important role in the packet
316 evolution and temporal dynamics of wave-particle interaction (see Figures 2,3).

317 Temporal dynamics of $\sigma_\mu(\Theta_L)$ in the linear regime at low Θ_L is also different for different cases (see
318 bottom row of Figure 5): σ_μ increases with time in Case I, decreases only slightly in Case II and remains
319 constant in Case III. The results of (Grach and Demekhov 2020a), on the contrary, show only an increase
320 in σ_μ with time for low pitch angles and higher energies (see Appendix there). The reason for such a
321 difference stems from the fact that the resonance points of such electrons are located near the leading edge
322 of the packet (Grach and Demekhov 2018b, 2020a). So, the resonant interaction with these particles will
323 be influenced by the dissipation of lower-frequency waves once the packet nears He^+ resonance. In Case
324 I, there is no dissipation during the simulation time; so, σ_μ increasing is due to wave packet propagation,
325 like in (Grach and Demekhov 2020a). In Cases II and III, $\sigma_\mu(\Theta_L)$ temporal dynamics is determined by
326 the wave packet dissipation, though amplitude modulation also can have a quantitative effect.

327 We should also note that particle trapping by the wave field leads to a significant change in Θ_L (up
328 to 40°) only in Case II (the case with minimum values of inhomogeneity parameter R and the longest
329 packet). In Cases I and III, pitch angle change as a result of trapping doesn't exceed 20° , mostly because
330 effective packet lengths are shorter in these cases. The similar results of particles detrapping due to short
331 packet effective lengths were observed in test particle simulations for whistler mode packets (Tao et al.
332 2012).

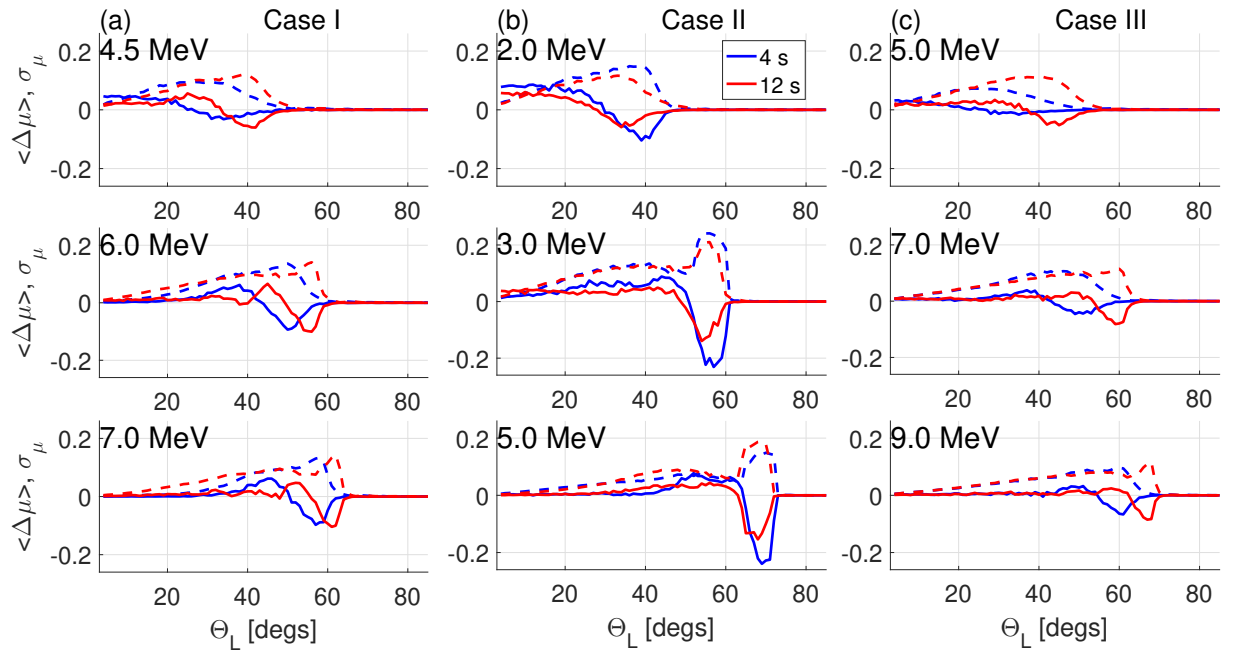


Figure 5. Phase averaged change in μ (solid lines) and root mean square deviation σ_μ (dashed lines) for different energies for Case I (a), II (b) and III (c) for $t - t_{\text{begin}} = 4$ s and $t - t_{\text{begin}} = 12$ s (blue and red lines, respectively).

333 **Precipitation mechanisms**

334 Let us analyze particle precipitation mechanisms during the entire simulation time. Following (Grach
335 and Demekhov 2020a), we plot the scattering pitch angle Θ_{Lsc} (equatorial pitch angles of precipitating
336 electrons before the last interaction with the wave packet) as a function of time. Figure 6 shows the
337 results for Case II, and the results for the other two cases are qualitatively similar.

338 As one can see from Figure 6, the maximum scattering pitch angle Θ_{Lsc} is about 30° . According to
339 previous analysis (see Figures 4, 5 and relevant discussion), for these pitch angles $R > 1$. Thus, of
340 nonlinear regimes only force bunching and/or nonlinear shift of the resonance point are possible.

341 Force bunching blocks precipitation from low pitch angles for lower energies (about one half of the
342 considered energy range). At the same time, when precipitation from low Θ_L is blocked by force bunching,
343 it is possible from higher Θ_L . Specifically, at $W_0 = 2$ MeV (Figure 6b), precipitation is blocked from
344 $\Theta_{Lsc} \leq 20^\circ$ (at early times) but is possible from Θ_{Lsc} up to 30° . This precipitation occurs in the regime
345 which is close to linear (with small influence of nonlinear shift of the resonance point). For higher energies,
346 when the effect of force bunching is absent (Figures 6e and f), $\Theta_{Lsc} \leq 10^\circ$. The range of blocked pitch
347 angles and maximum Θ_{Lsc} have a maximum over energy; for entirely linear precipitation the range of
348 Θ_{Lsc} decreases with energy.

349 Trapping by the wave field can't directly cause precipitation, because it occurs at high pitch angles and
350 $|\Delta\Theta_L| < \Theta_{L0} - \Theta_{Lc}$. To analyze indirect influence of trapping, we plot the maximum change (decrease)
351 in Θ_L of precipitating particles over their trajectories $|\Delta\Theta_L|_{\max}^{\text{lost}}$. The results for Case II are shown in
352 Figure 7. For lower energies (Figures 7a and b) the trapping is impossible (see Figure 4e), and $|\Delta\Theta_L|_{\max}^{\text{lost}}$
353 has roughly the same value as the change which leads directly to precipitation. For intermediate energies
354 (Figures 7c and 7d) particles that have been trapped along their trajectory can make up a significant
355 part of precipitating particles. For higher energies (Figure 7f), there are no trapped particles in the loss
356 cone, despite the fact that for these energies trapping is the most effective. It happens because trapping
357 takes place for $\Theta_L \geq 60^\circ$, while in rather wide range $\Theta_L \leq 40^\circ$ the wave-particle interaction is linear
358 with small σ_μ (see bottom row of Figure 5). Thus, trapped particles don't have enough time to reach the
359 loss cone due to diffusion after they leave the trapping region.

360 Figures 6 and 7 also demonstrate the influence of the initial particle distribution in space at the beginning
361 of the simulation. As one can see, this influence disappears after 4 – 8 bounce oscillations (approximately

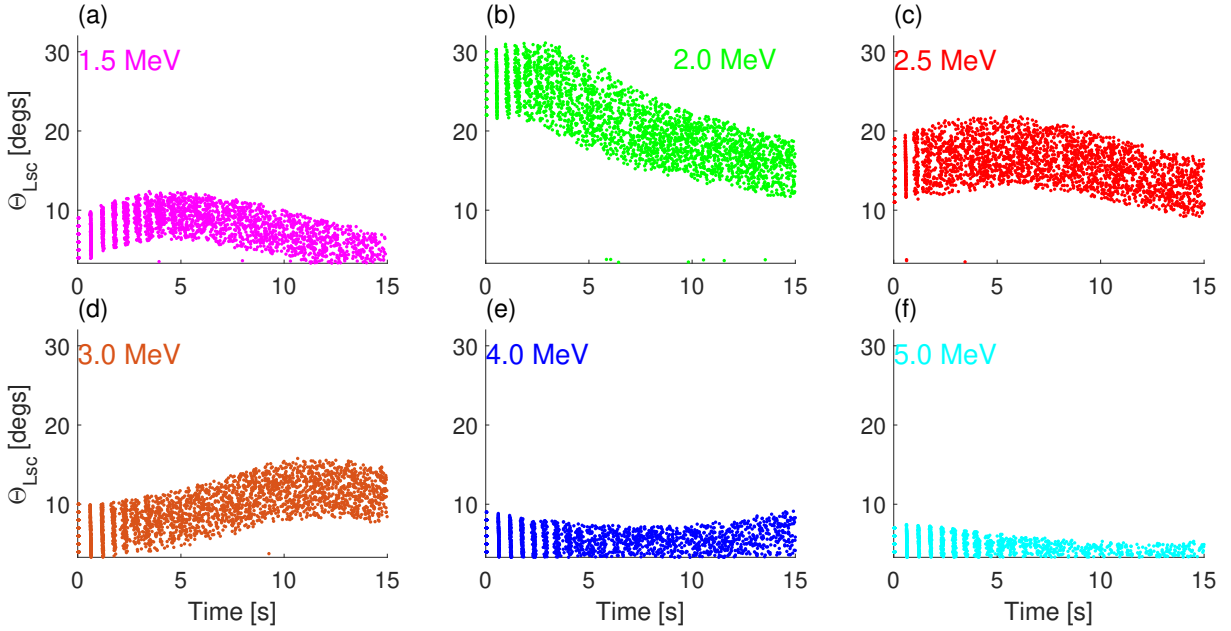


Figure 6. Equatorial pitch angles Θ_{Lsc} of precipitating electrons before the last interaction with the wave packet as a function of time for Case II. Time is counted from the beginning of simulation and corresponds to particle exiting the wave packet.

³⁶² $2 \div 5$ seconds).

³⁶³ Temporal dynamics of Θ_{Lsc} is complicated, different for different energies even within one case and more
³⁶⁴ diverse than for a model packets considered in (Grach and Demekhov 2020a). When nonlinear effects
³⁶⁵ are strong ($W_0 < 4$ MeV, Figures 6a–d), the difference from the earlier results is mostly due to longer
³⁶⁶ simulation time. When precipitation is linear or almost linear ($W_0 \geq 4$ MeV, Figures 6e and f), the range
³⁶⁷ of precipitation pitch angles has a slight minimum or decreases with time; for a model wave packet with
³⁶⁸ Gaussian amplitude profile, precipitation pitch angle range increases with time for linear precipitation
³⁶⁹ (Grach and Demekhov 2020a).

³⁷⁰ This difference is explained by the fact that for particles with higher energies and low pitch angles
³⁷¹ resonant interaction is influenced by dissipation of the lower-frequency waves once the packet nears the
³⁷² He^+ resonance. Also, spatial amplitude profiles for Case II are different from Gaussian one (see Figure 2b);
³⁷³ this amplitude modulation is not strong enough to cause qualitative difference for interaction regimes at
³⁷⁴ any given time, but can have quantitative effect.

³⁷⁵ For Cases I and III, generation of higher-frequency waves might influence Θ_{Lsc} temporal dynamics. These
³⁷⁶ dynamics is roughly the same as temporal dynamics of precipitating flux, that is discussed below.

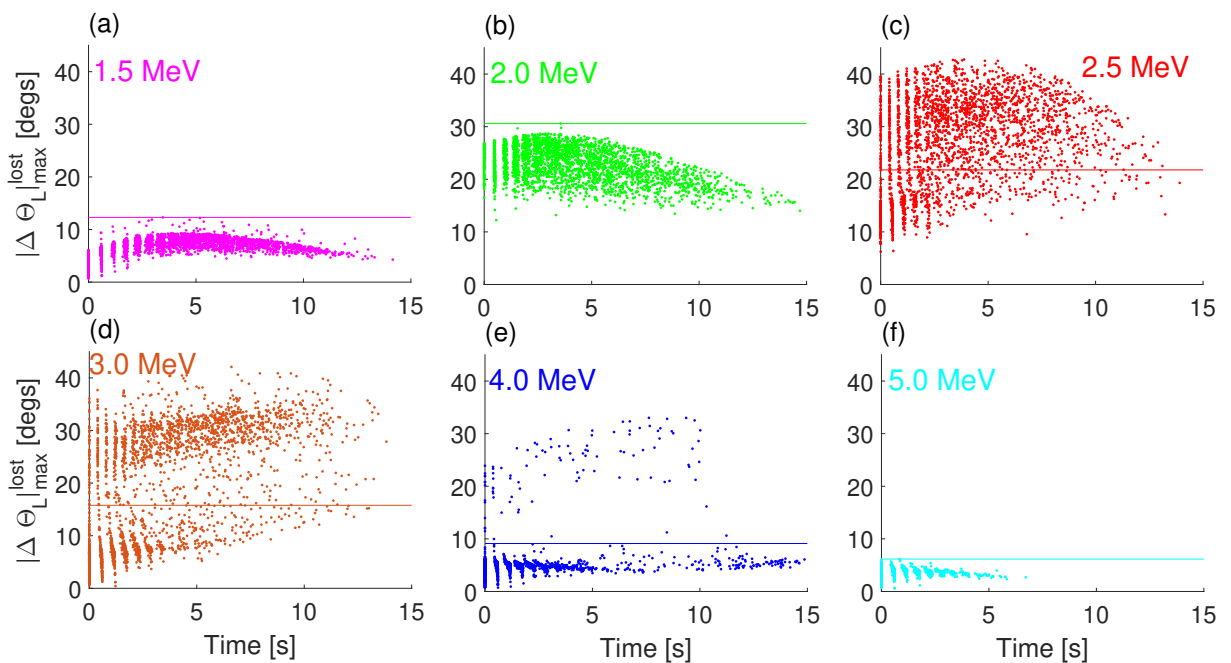


Figure 7. The maximum change in equatorial pitch angle over the trajectory for precipitating electrons. Case II, time is counted from the beginning of simulation and corresponds to particle exiting the wave packet after the maximum change has occurred. Horizontal line shows the maximum change for the precipitation itself.

377 **Evolution of the Distribution Function**

378 To analyze the simulation results in terms of particle distribution function and for correct analysis of
 379 precipitating fluxes, we have to establish the connection between the distribution function $\Phi_{\Theta_L}(\Theta_L)$ and
 380 the distribution of the test particles in the phase space. As in (Grach and Demekhov 2020a) we use the
 381 following normalization (Bespalov and Trakhtengerts 1986; Trakhtengerts and Rycroft 2008):

$$N = \int n(z) \frac{B_{0m}}{B_0(z)} dz. \quad (11)$$

382 Here N is the number of particles in a geomagnetic flux tube with a unit cross section at the ionosphere,
 383 $n(z) = \int f d^3 p = \int f \sin \Theta d\Theta p^2 dp d\Psi$ is the local number density, f is the local particle distribution
 384 function averaged over gyrophases, Θ is the local pitch angle, p is particle momentum and B_{0m} is the
 385 maximum field for the given geomagnetic field line. The distribution function f can be averaged over
 386 bounce oscillations and integrated over particle momentum (taking into account that the electron energy
 387 is conserved with a high accuracy) and over phases and thus we obtain particles distribution in equatorial
 388 pitch angles $\Phi_{\Theta_L}(\Theta_L)$.

389 We can also express N via the number of test particles in the simulation, N_p :

$$N = \frac{v_0 \bar{T}_B}{2\mu_c} \beta_V N_p, \quad (12)$$

390 where v_0 is particle velocity (which stays constant during the interaction), $\mu_c = \sin^2 \Theta_{Lc}$ corresponds to
 391 the loss cone, $\bar{T}_B = \int T_B(\mu) d\mu$, β_V is the normalization constant, and N_p is the number of test particles
 392 in the simulation.

393 Using (11) and (12), we can write the connection between distribution function Φ_{Θ_L} and distribution of
 394 the test particles in the phase space as follows:

$$\Phi_{\Theta_L} = \frac{\Delta N_p}{\Delta \Theta_L} \frac{\bar{T}_B}{T_B} \frac{\beta_V}{\sin(2\Theta_L)}; \quad (13)$$

395 Here ΔN_p is the number of test particles having the pitch angle Θ_L within the range $\Delta \Theta_L$.

396 We also assign a specific weight to each test particle to ensure that the initial particle distribution
 397 $\Phi_{\Theta_L}|_{t=t_{\text{begin}}}$ is constant. More details can be found in the Appendix of (Grach and Demekhov 2020a).

398 We divide the total simulation time 15 s in 26 intervals $\{\Delta t_i\} = t_{i+1} - t_i$, $i = 0, 1, \dots, 26$, $t_0 = t_{\text{begin}}$,
 399 $t_{26} = t_{\text{end}}$, where $\Delta t_0 = \Delta t_{25} = 0.3$ s and the other intervals $\Delta t_{0 < i < 25} = 0.6$ s. The value 0.6 s
 400 corresponds to the bounce period of particles close to the loss cone: $T_B(\Theta_L = \Theta_{Lc}) \approx 0.6\text{--}0.62$ s. The

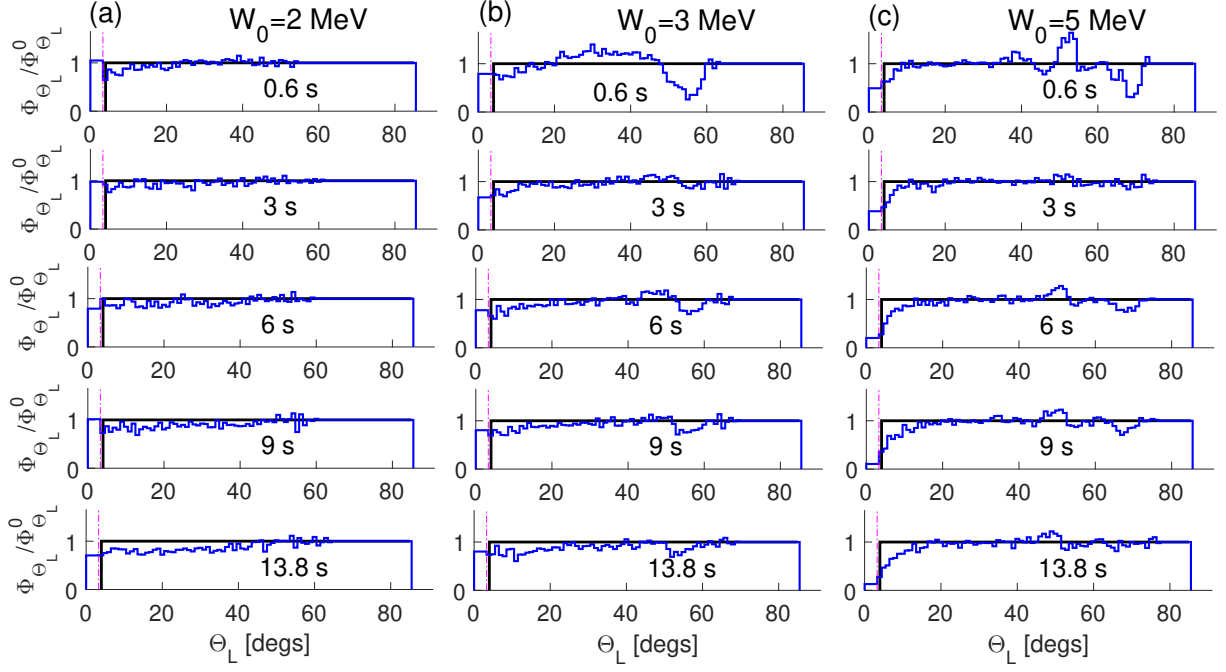


Figure 8. Evolution of distribution function. Case II, time is counted from the beginning of simulation. Initial distribution is shown in black, the magenta line corresponds to the loss cone.

401 first interval is chosen shorter, because at $t_0 = t_{\text{begin}}$ the particle ensemble is located near the equator;
 402 the time $\Delta t_0 = 0.3$ s is long enough that all particles precipitated after the first pass through the packet
 403 will reach the ionosphere and short enough that all other particles during Δt_0 will pass the wave packet
 404 in the resonant direction only once. In the further analysis, both Δt_0 and Δt_{25} will be ignored.
 405 We average the particle distribution function over the intervals Δt_i and attribute the obtained result to
 406 the time $\tau_i = (t_{i+1} + t_i)/2$ (the middle of the interval Δt_i). We use the grid in Θ_L which is not fine
 407 enough to ensure distribution function resolution within the loss cone, so in the loss cone the distribution
 408 function has one value, $\Phi_{\Theta_L}^c$.
 409 Figure 8 shows the evolution of distribution function for 3 values of energy in Case II. These energies
 410 represent three typical patterns of wave-particle interaction in Case II; Cases I and III also demonstrate
 411 the similar patterns.

412 For $W_0 = 2$ MeV (lower energies), the distribution function is close to isotropic for $\Theta_L \leq 60^\circ$ (there is
 413 no resonant interaction for higher Θ_L , so the distribution function remains undisturbed). The value of
 414 Φ_{Θ_L} slowly decreases with time from the initial value $\Phi_{\Theta_L}^0$ to approximately $0.8\Phi_{\Theta_L}^0$.
 415 For $W_0 = 3$ MeV (intermediate energies), the distribution function is close to isotropic up to $\Theta_L \approx 20^\circ -$
 416 30° and then there are noticeable variations with a maximum in the vicinity of 40° and a minimum in

417 the vicinity of 50° . These variations are caused by phase bunching and trapping.

418 For $W_0 = 5$ MeV (higher energies), the distribution function increases from $\Phi_{\Theta_L}^c \approx (0\text{--}0.5)\Phi_{\Theta_L}^0$ in the loss
419 cone to the initial value $\Phi_{\Theta_L}^0$ at $\Theta_L \approx 20^\circ$. Noticeable variations, associated with phase bunching and
420 trapping by the wave field, take place in the area $\Theta_L \approx 40^\circ\text{--}70^\circ$ and thus don't influence the precipitation.
421 The behavior of the distribution function in the vicinity of the loss cone is roughly the same as for the
422 model Gaussian packet in (Grach and Demekhov 2020a). Trapping by the wave field is not effective
423 for Gaussian packet and particle ensemble considered in (Grach and Demekhov 2020a), so noticeable
424 variations, associated with trapping, were present only for a model packet with flat amplitude profile.

425 Precipitating Flux

426 For the further analysis, we normalize the precipitating fluxes $S_{\text{pr}}^{\text{num}}$, directly corresponding to the
427 numerical simulation results, to the flux $S_{\text{pr}}^{\text{SD}}$ in the limiting case of strong diffusion. In this case the
428 loss cone is filled continuously and distribution function is isotropic; the precipitating flux takes the
429 limiting value equal to the trapped flux (Kennel and Petschek 1966; Bespalov and Trakhtengerts 1986;
430 Trakhtengerts and Rycroft 2008):

$$S_{\text{pr}}^{\text{SD}} = \frac{N\mu_c}{T_B}. \quad (14)$$

431 Here N is the number of particles in geomagnetic field tube with a unit cross section at the ionosphere
432 (11), (12). The simulated precipitating flux is evaluated as:

$$S_{\text{pr}}^{\text{num}}(\tau_i) = \frac{N\delta N_p}{\Delta t_i}. \quad (15)$$

433 Here $\delta N_p = N_{\text{p lost}}/N_p$ is the relative number of test particles, precipitated during time interval Δt_i , τ_i
434 and Δt_i are described above.

435 Dependencies of the normalized precipitating fluxes $\tilde{S} = S_{\text{pr}}^{\text{num}}/S_{\text{pr}}^{\text{SD}}$ on the time and energy are shown
436 in Figure 9. Precipitating fluxes \tilde{S}_{av} , averaged over the whole simulation time, as well as maximum and
437 minimum values, are shown in Figure 10.

438 The energy dependence of time-averaged fluxes is similar for all three cases. At the lowest energy,
439 $\tilde{S}_{\text{av}} \approx 0.4\text{--}0.6$, then it increases to $\tilde{S}_{\text{av}} \approx 1$ and is nearly constant for an interval about 1 MeV ($W_0 = 4\text{--}$
440 5 MeV for Case I; $W_0 = 2\text{--}3$ MeV for Case II; $W_0 = 4.5\text{--}5.5$ MeV for Case III) and then decreases, to
441 values $\tilde{S}_{\text{av}} \leq 0.25$ at the right boundary of the energy range.

442 The maximum values of precipitating fluxes correspond to the case of strong diffusion, i.e. to an almost

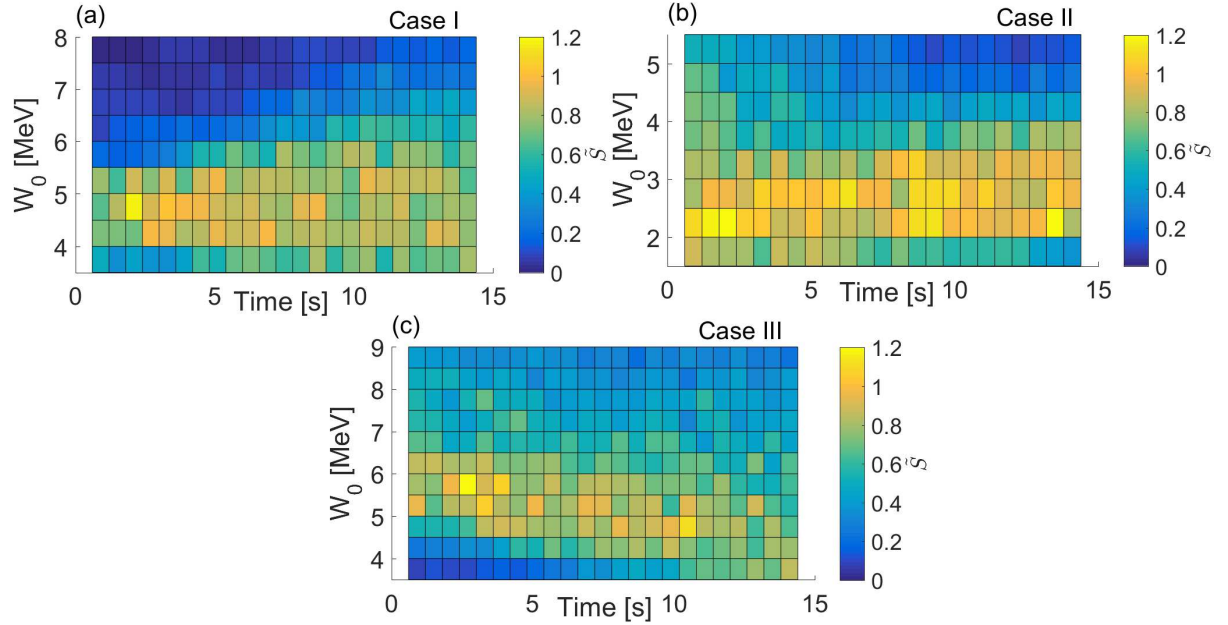


Figure 9. Temporal dynamics of normalized precipitating fluxes for Case I (a), II (b) and III (c)

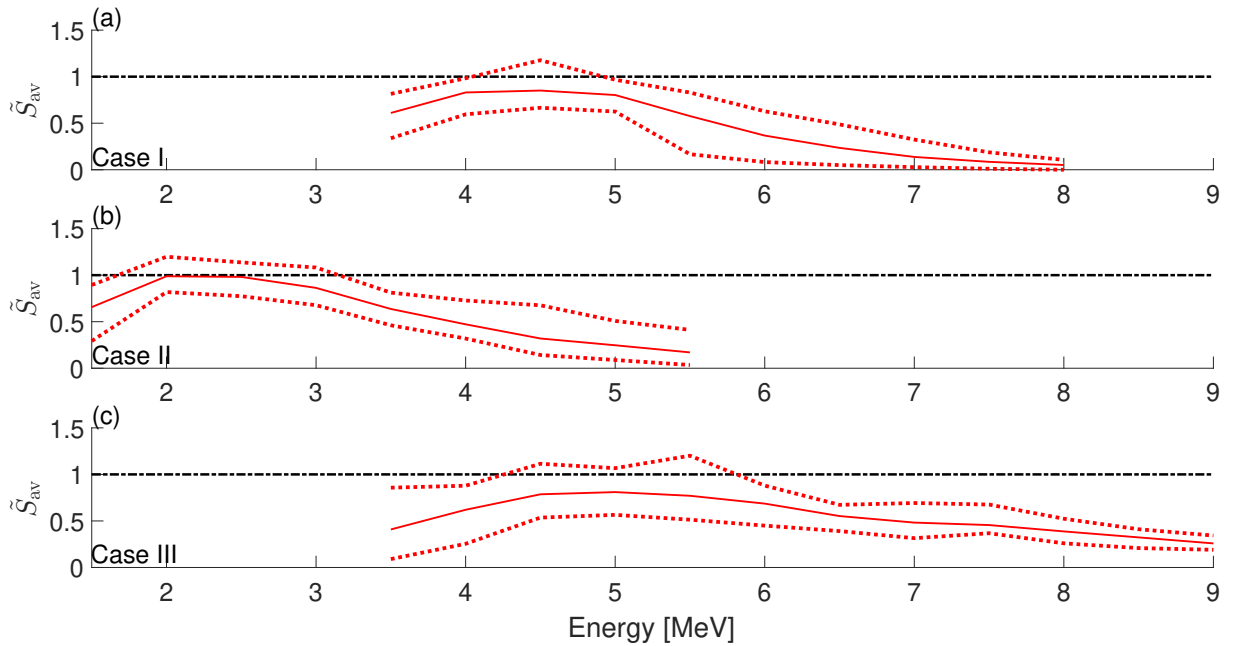


Figure 10. Normalized precipitating fluxes, averaged (solid lines), maximized (dotted lines) and minimized (dotted lines) over the simulation time, for Case I (a), II (b) and III (c).

443 isotropic distribution function in the vicinity of the loss cone (see Figure 8). These cases correspond
444 to the strongest interaction at $\Theta_L < 40^\circ$, i.e. the most effective force bunching, the highest values of
445 precipitating pitch angles Θ_{Lsc} and the widest range of Θ_{Lsc} (see Figures 6b, 6c and 6d). In Case II,
446 there is an energy range ($2.5 \text{ MeV} \leq W_0 \leq 3.0 \text{ MeV}$), for which $S_{\text{pr}}^{\text{num}}/S_{\text{pr}}^{\text{SD}} \sim 1$ and trapping by the wave
447 influences the precipitation (see Figures 7c and 7d). In Cases I and III for energies corresponding to
448 maximum fluxes trapping is not possible (see Figures 4e and 4f).

449 The time dependence for maximum precipitating fluxes is not significant: fluxes oscillate near the average
450 value. For lower and higher energies, when $S_{\text{pr}}^{\text{num}}/S_{\text{pr}}^{\text{SD}} < 1$, temporal dynamics of the fluxes is determined
451 by generation of higher-frequency waves at the trailing edge, dissipation of the lower-frequency waves at
452 the leading edge and propagation effects. For particles with lower energies, resonance points are located
453 closer to the trailing edge (for rising tone packets, see (Grach and Demekhov 2018a, 2020a)), thus the
454 resonant interaction is influenced by the generation of higher-frequency waves. When the generation takes
455 place during the simulation, precipitating fluxes for lower energies increase with time (Cases I and III);
456 when the generation is finished and wave packet propagates away from the equator, precipitating fluxes
457 for lower energies decrease with time (Case II and model Gaussian packet in (Grach and Demekhov
458 2020a)). For particles with higher energies and low pitch angles (which determine the precipitation),
459 resonant interaction, on the contrary, is influenced by the dissipation of lower-frequency waves at the
460 leading edge. Thus, before the dissipation starts, precipitating fluxes for higher energies increase with
461 time (Case I and model Gaussian packet in (Grach and Demekhov 2020a)) due to propagation effects;
462 when the dissipation takes place precipitating fluxes for higher energies either fluctuate near an average
463 value (Case III) or decrease with time (Case II).

464 It's also important to note that the temporal dynamics of the precipitating fluxes in the linear regime
465 (higher energies) agrees with temporal dynamics of σ_μ (see Figure 5 and relevant discussion) and thus
466 with temporal dynamics of diffusion coefficients. The decrease of \tilde{S}_{av} with energy once the precipitation
467 becomes linear is slowest for the case with lowest frequencies at the leading edge (Case III). Under similar
468 wave amplitudes lower frequencies at the leading edge lead to smaller values of R for low pitch angles
469 and higher energies, which in turn leads to larger σ_μ .

470 Note that Cases I and II actually belong to the same wave packet (element 14) with strong amplitude
471 modulation and simulation for Case II starts 20 s after simulation for Case I ends (see Figure 2). Thus, for

472 element 14 we can assume a significant change in energy spectrum of precipitated particles on a time scale
473 about 30 s. Within one simulation (15 s) there also can be a slight change of precipitated particles energy
474 spectrum, caused by the wave packet evolution: the flux maximum on energy can become smoother (Case
475 I), more pronounced (Case II) or shift to lower energies (Case III).

476 The temporal dynamics of precipitated fluxes and the energy spectrum of precipitating particles is
477 generally in qualitative agreement with the results of (Kubota and Omura 2017), corresponding to the
478 case when trapping doesn't cause direct precipitation (the case with low cold plasma density).

479 **Summary**

480 We have studied the resonant interaction of relativistic electrons with EMIC wave packets within one
481 event (11:50–13:50 UT, 14 September 2017, Van Allen Probe B). The considered wave packets have rising
482 tone within proton band and amplitudes up to 1.2 nT.

483 As a result of interaction with the wave packets under consideration, electrons with energies of 1.5–9 MeV
484 can effectively precipitate into the loss cone. For particles with energies 2–5 MeV (depending on the
485 wave packet and time interval), the precipitating flux is close to the limiting value corresponding to the
486 strong diffusion regime.

487 The influence of a realistic wave packet structure brings the following specific features in the interaction,
488 compared with idealized cases considered earlier (Grach and Demekhov 2020a).

489 For the considered short time intervals, the approximation of each local amplitude maximum of the wave
490 packet by a Gaussian amplitude profile and a linear frequency drift gives a satisfactory description of the
491 resonant interaction dynamics. At the same time, generation of higher-frequency waves at the packet
492 trailing edge near the equator and dissipation of lower-frequency waves in the He^+ gyroresonance region
493 at the leading edge can play an important role.

494 Generation of higher-frequency waves mostly influences interaction for electrons with lower energies
495 and/or higher equatorial pitch angles, i.e. the particles, for which nonlinear interaction takes place.

496 As long as the higher-frequency parts of the wave packet are generated near the equator with high
497 enough amplitudes, the precipitating flux at lower energies increases. Once the generation stops and the
498 wave propagates away from the equator, the corresponding precipitating flux decreases.

499 Dissipation of lower-frequency waves mostly affects interaction for particles with higher energies and low

500 equatorial pitch angles, i.e. linear interaction. Once the dissipation starts, precipitating flux for particles
501 with higher energies decreases with time. If there is no dissipation in the considered time interval,
502 precipitating flux for higher energy particles (linear precipitation) will increase with time.

503 The amplitude modulation of the wave packet leads to a significant change of energy spectrum of
504 precipitated particles during short time. Specifically, for element 14 of the considered event (three local
505 amplitude maxima), the energy with maximum precipitating flux decreases from $W_0 \approx 4.5$ MeV to
506 $W_0 \approx 2.5$ MeV during 30 s, while the element itself exists for about 120 s.

507 The main nonlinear effects, which affect the precipitation, are the force bunching and nonlinear shift
508 of the resonance point. Force bunching blocks precipitation for particles with low pitch angles, up to
509 $\Theta_L \approx 20^\circ$. At the same time the precipitation can exist from a noticeable range of higher $\Theta_L \approx 10^\circ\text{--}30^\circ$.
510 This situation corresponds to maximum precipitating fluxes.

511 Particle trapping by the wave field can indirectly influence precipitation for some energies, but this
512 influence is not crucial for the considered parameters. Effective precipitation due to trapping and directed
513 scattering is possible for longer and higher-amplitude wave packets (amplitudes up to 14 nT are observed
514 (Kitahara and Katoh 2019)) and also for higher cold plasma density (Kubota and Omura 2017; Grach
515 and Demekhov 2018a,b).

516 In summary, for EMIC wave packets with amplitudes around 1 nT nonlinear effects play an important
517 role in the formation of precipitating fluxes, even in the cases when wave packets are short and trapping
518 by the wave field is not effective. Model wave packets with main parameters based on observations give
519 a satisfactory description of precipitation dynamics, but real fine structure of a wave packet influences
520 actual values of precipitating fluxes very significantly. It may be of interest to study other specific cases
521 corresponding to real observations, and this will be a subject of future work.

522 **Declarations**

523 **Availability of data and materials**

524 Van Allen Probe data used in this paper can be found in the EMFISIS (<https://emfisis.physics.uiowa.edu/data/index>).

525 **Competing interests**

526 The authors declare that they have no competing interests.

527 **Funding**

528 The work of V.S. Grach (numerical simulations) in this study was supported by the Russian Science
529 Foundation, grant No. 19-72-10111. The work of A.G. Demekhov (model formulation and interpreting
530 of the results) was carried out as a part of State Assignment of Ministry of Education and Science of the
531 Russian Federation, project No. 0030-2021-0002.

532 **Authors' contributions**

533 VSG: numerical simulations, structure and strategy of the paper, and writing the paper. AGD: structure
534 and strategy of the paper, model formulation and interpreting of the results, editing of the paper. AVL:
535 processing of EMFISIS data and distinguishing of discrete elements from the dynamic spectrum. All
536 authors read and approved the final manuscript.

537 **Acknowledgments**

538 The authors would like to thank the designers of Van Allen Probes and developers of the instruments
539 (EMFISIS — Craig Kletzing) for the open access to the data.

540 **References**

- 541 Albert, J. M. (1993), Cyclotron resonance in an inhomogeneous magnetic field, Physics of Fluids B,
542 5(8), 2744–2750, doi:10.1063/1.860715.
- 543 Albert, J. M. (2000), Gyroresonant interactions of radiation belt particles with a monochromatic
544 electromagnetic wave, J. Geophys. Res. Space Phys., 105(A9), 21,191–21,209,
545 doi:10.1029/2000JA000008.
- 546 Albert, J. M., and J. Bortnik (2009), Nonlinear interaction of radiation belt electrons with
547 electromagnetic ion cyclotron waves, Geophys. Res. Lett., 36(12), L12110, doi:10.1029/2009GL038904.
- 548 Artemyev, A. V., D. Mourenas, O. V. Agapitov, D. L. Vainchtein, F. S. Mozer, and V. Krasnoselskikh
549 (2015), Stability of relativistic electron trapping by strong whistler or electromagnetic ion cyclotron
550 waves, Physics of Plasmas, 22(8), 082901, doi:10.1063/1.4927774.
- 551 Artemyev, A. V., A. I. Neishtadt, A. A. Vasiliev, and D. Mourenas (2017), Probabilistic approach to
552 nonlinear wave-particle resonant interaction, Phys. Rev. E, 95(2), 023204,

- 553 doi:10.1103/PhysRevE.95.023204.
- 554 Bespalov, P. A., and V. Y. Trakhtengerts (1986), The cyclotron instability in the Earth radiation belts,
555 in *Reviews of Plasma Physics*, vol. 10, edited by M. A. Leontovich, pp. 155–293, Plenum Publ., N.Y.
- 556 Demekhov, A. (2007), Recent progress in understanding Pc1 pearl formation, *Journal of Atmospheric*
557 *and Solar-Terrestrial Physics*, 69, 1609–1622, doi:10.1016/j.jastp.2007.01.014.
- 558 Demekhov, A. G., V. Y. Trakhtengerts, M. J. Rycroft, and D. Nunn (2006), Electron acceleration in the
559 magnetosphere by whistler-mode waves of varying frequency, *Geomagnetism and Aeronomy*, 46,
560 711–716, doi:10.1134/S0016793206060053.
- 561 Demekhov, A. G., V. Y. Trakhtengerts, M. Rycroft, and D. Nunn (2009), Efficiency of electron
562 acceleration in the Earth’s magnetosphere by whistler mode waves, *Geomagnetism and Aeronomy*,
563 49(1), 24–29, doi:10.1134/S0016793209010034.
- 564 Engebretson, M. J., A. Keiling, K.-H. Fornacon, C. A. Cattell, J. R. Johnson, J. L. Posch, S. R. Quick,
565 K.-H. Glassmeier, G. K. Parks, and H. Rème (2007), Cluster observations of Pc 1 2 waves and
566 associated ion distributions during the October and November 2003 magnetic storms, *Planetary and*
567 *Space Science*, 55, 829–848, doi:10.1016/j.pss.2006.03.015.
- 568 Engebretson, M. J., J. L. Posch, A. M. Westerman, N. J. Otto, J. A. Slavin, G. Le, R. J. Strangeway,
569 and M. R. Lessard (2008), Temporal and spatial characteristics of pc1 waves observed by st5, *Journal*
570 *of Geophysical Research: Space Physics*, 113(A7), a07206, doi:10.1029/2008JA013145.
- 571 Grach, V. S., and A. G. Demekhov (2018a), Resonance interaction of relativistic electrons with
572 ion-cyclotron waves. i. specific features of the nonlinear interaction regimes, *Radiophysics and*
573 *Quantum Electronics*, 60(12), 942–959, doi:10.1007/s11141-018-9860-0.
- 574 Grach, V. S., and A. G. Demekhov (2018b), Resonant interaction of relativistic electrons with
575 electromagnetic ion–cyclotron waves. ii. integral parameters of interaction regimes, *Radiophysics and*
576 *Quantum Electronics*, 61(6), 389–401, doi:10.1007/s11141-018-9900-9.
- 577 Grach, V. S., and A. G. Demekhov (2020a), Precipitation of relativistic electrons under resonant
578 interaction with electromagnetic ion cyclotron wave packets, *J. Geophys. Res. Space Phys.*, 125(2),
579 e2019JA027358, doi:10.1029/2019JA027358.
- 580 Grach, V. S., and A. G. Demekhov (2020b), Regimes of resonant interactions of electrons with auroral
581 kilometric radiation, *Radiophysics and Quantum Electronics*, 63(3), 157–176,
582 doi:10.1007/s11141-021-10043-5.

- 583 Jordanova, V. K., J. Albert, and Y. Miyoshi (2008), Relativistic electron precipitation by emic waves
584 from self-consistent global simulations, *Journal of Geophysical Research: Space Physics*, 113(A3),
585 a00A10, doi:10.1029/2008JA013239.
- 586 Kangas, J., A. Guglielmi, and O. Pokhotelov (1998), Morphology and physics of short-period magnetic
587 pulsations, *Space Science Reviews*, 83, 435–512.
- 588 Karpman, V. I., Y. N. Istomin, and D. R. Shklyar (1974), Nonlinear theory of a quasimonochromatic
589 whistler mode packet in inhomogeneous plasma, *Plasma Phys.*, 16(8), 685–703,
590 doi:10.1088/0032-1028/16/8/001.
- 591 Kennel, C. F., and H. E. Petschek (1966), Limit on Stably Trapped Particle Fluxes, *J. Geophys. Res.*,
592 71(1), 1–28, doi:10.1029/JZ071i001p00001.
- 593 Kitahara, M., and Y. Katoh (2019), Anomalous Trapping of Low Pitch Angle Electrons by Coherent
594 Whistler Mode Waves, *Journal of Geophysical Research (Space Physics)*, 124(7), 5568–5583,
595 doi:10.1029/2019JA026493.
- 596 Kubota, Y., and Y. Omura (2017), Rapid precipitation of radiation belt electrons induced by emic
597 rising tone emissions localized in longitude inside and outside the plasmapause, *J. Geophys. Res.*
598 *Space Phys.*, 122(1), 293–309, doi:10.1002/2016JA023267.
- 599 Larchenko, A. V., A. G. Demekhov, and B. V. Kozelov (2019), The Parameterization Method of
600 Discrete VLF Chorus Emissions, *Radiophysics and Quantum Electronics*, 62(3), 159–173,
601 doi:10.1007/s11141-019-09964-z.
- 602 Li, W., and M. K. Hudson (2019), Earth's Van Allen Radiation Belts: From Discovery to the Van Allen
603 Probes Era, *Journal of Geophysical Research (Space Physics)*, 124(11), 8319–8351,
604 doi:10.1029/2018JA025940.
- 605 Lundin, B. V., and D. R. Shkliar (1977), Interaction of electrons with low transverse velocities with
606 VLF waves in an inhomogeneous plasma, *Geomagnetism and Aeronomy*, 17, 246–251.
- 607 Lyons, L. R., and R. M. Thorne (1973), Equilibrium structure of radiation belt electrons, *Journal of*
608 *Geophysical Research*, 78(13), 2142–2149, doi:10.1029/JA078i013p02142.
- 609 Mauk, B. H., N. J. Fox, S. G. Kanekal, R. L. Kessel, D. G. Sibeck, and A. Ukhorskiy (2013), *Science*
610 Objectives and Rationale for the Radiation Belt Storm Probes Mission, *Space Science Reviews*,
611 179(1-4), 3–27, doi:10.1007/s11214-012-9908-y.
- 612 Millan, R. M., and R. Thorne (2007), Review of radiation belt relativistic electron losses, *Journal of*

- 613 Atmospheric and Solar-Terrestrial Physics, 69(3), 362 – 377, doi:10.1016/j.jastp.2006.06.019.
- 614 Morley, S. K., R. H. W. Friedel, T. E. Cayton, and E. Noveroske (2010), A rapid, global and prolonged
615 electron radiation belt dropout observed with the global positioning system constellation,
616 Geophysical Research Letters, 37(6), doi:10.1029/2010GL042772.
- 617 Nakamura, S., Y. Omura, C. Kletzing, and D. N. Baker (2019), Rapid Precipitation of Relativistic
618 Electron by EMIC Rising-Tone Emissions Observed by the Van Allen Probes, Journal of Geophysical
619 Research (Space Physics), 124(8), 6701–6714, doi:10.1029/2019JA026772.
- 620 Omura, Y., and Q. Zhao (2012), Nonlinear pitch angle scattering of relativistic electrons by emic waves
621 in the inner magnetosphere, Journal of Geophysical Research: Space Physics, 117(A8),a08227,
622 doi:10.1029/2012JA017943. .
- 623 Omura, Y., and Q. Zhao (2013), Relativistic electron microbursts due to nonlinear pitch angle
624 scattering by emic triggered emissions, Journal of Geophysical Research: Space Physics, 118(8),
625 5008–5020, doi:10.1002/jgra.50477.
- 626 Pickett, J. S., B. Grison, Y. Omura, M. J. Engebretson, I. Dandouras, A. Masson, M. L. Adrian,
627 O. Santolík, P. M. E. Décréau, N. Cornilleau-Wehrlin, and D. Constantinescu (2010), Cluster
628 observations of EMIC triggered emissions in association with Pc1 waves near Earth’s plasmapause,
629 Geophysical Research Letters, 37, L09104, doi:10.1029/2010GL042648.
- 630 Shprits, Y. Y., L. Chen, and R. M. Thorne (2009), Simulations of pitch angle scattering of relativistic
631 electrons with mlt-dependent diffusion coefficients, J. Geophys. Res. Space Physics, 114(A3),
632 A03,219, doi:10.1029/2008JA013695.
- 633 Summers, D., and R. M. Thorne (2003), Relativistic electron pitch-angle scattering by electromagnetic
634 ion cyclotron waves during geomagnetic storms, Journal of Geophysical Research: Space Physics,
635 108(A4), 1143, doi:10.1029/2002JA009489.
- 636 Tao, X., J. Bortnik, R. M. Thorne, J. M. Albert, and W. Li (2012), Effects of amplitude modulation on
637 nonlinear interactions between electrons and chorus waves, Geophys. Res. Lett., 39(6), L06102,
638 doi:10.1029/2012GL051202.
- 639 Thorne, R. M., and C. F. Kennel (1971), Relativistic electron precipitation during magnetic storm main
640 phase, Journal of Geophysical Research, 76(19), 4446–4453, doi:10.1029/JA076i019p04446.
- 641 Trakhtengerts, V. Y., and M. J. Rycroft (2000), Whistler-electron interactions in the magnetosphere:
642 new results and novel approaches, Journal of Atmospheric and Solar-Terrestrial Physics, 62(17-18),

- 643 1719–1733, doi:10.1016/S1364-6826(00)00122-X.
- 644 Trakhtengerts, V. Y., and M. J. Rycroft (2008), Whistler and Alfvén mode cyclotron masers in space,
645 Cambridge Atmospheric and Space Sciences Series, Cambridge University Press, New York.
- 646 Tverskoy, B. A. (1969), Main mechanisms in the formation of the Earth's radiation belts., *Reviews of*
647 *Geophysics and Space Physics*, 7, 219–231, doi:10.1029/RG007i001p00219.
- 648 Zhang, X. J., R. Thorne, A. Artemyev, D. Mourenas, V. Angelopoulos, J. Bortnik, C. A. Kletzing,
649 W. S. Kurth, and G. B. Hospodarsky (2018), Properties of Intense Field-Aligned Lower-Band Chorus
650 Waves: Implications for Nonlinear Wave-Particle Interactions, *Journal of Geophysical Research*
651 (*Space Physics*), 123(7), 5379–5393, doi:10.1029/2018JA025390.

Figures

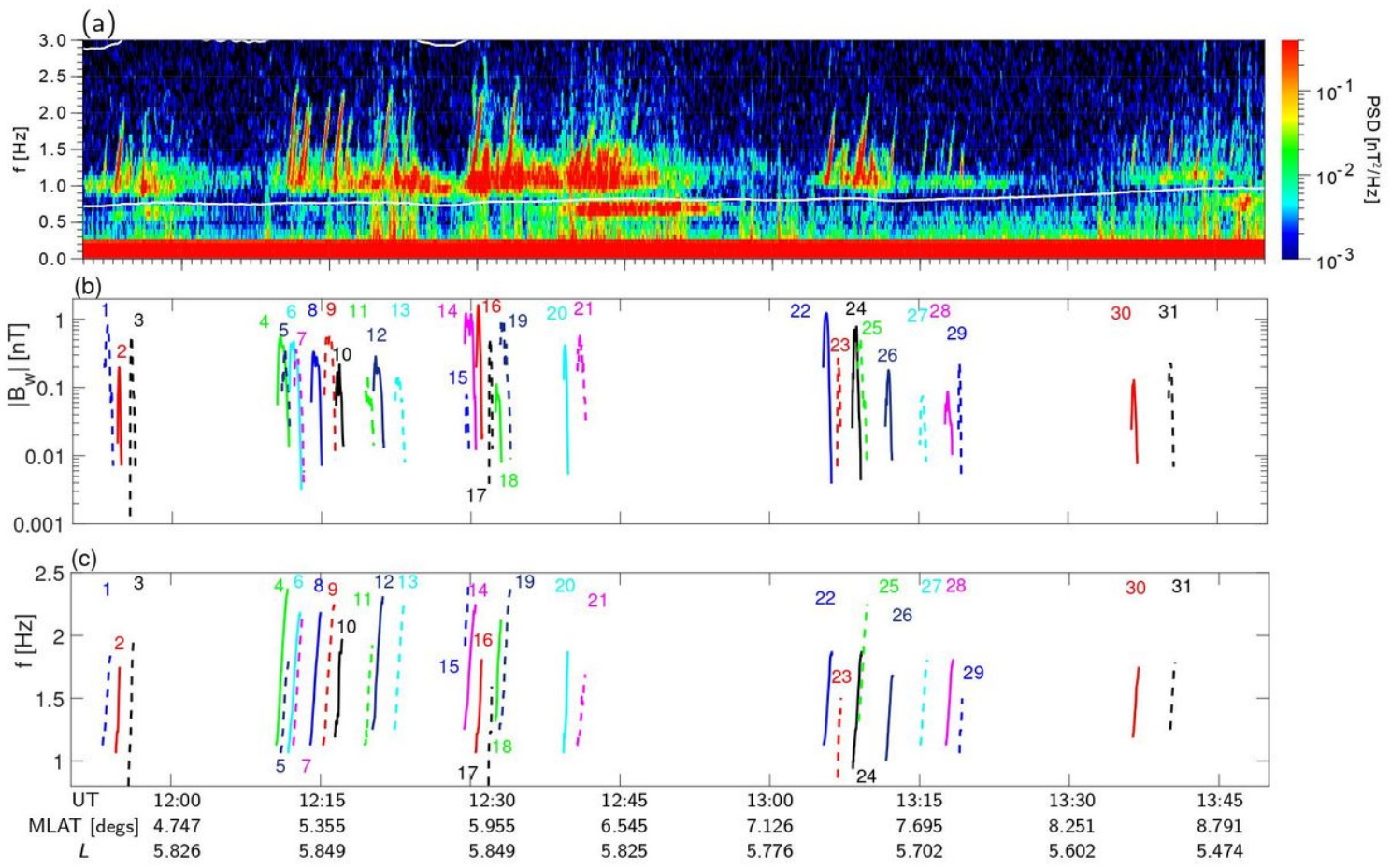


Figure 1

Please see the Manuscript PDF file for the complete figure caption

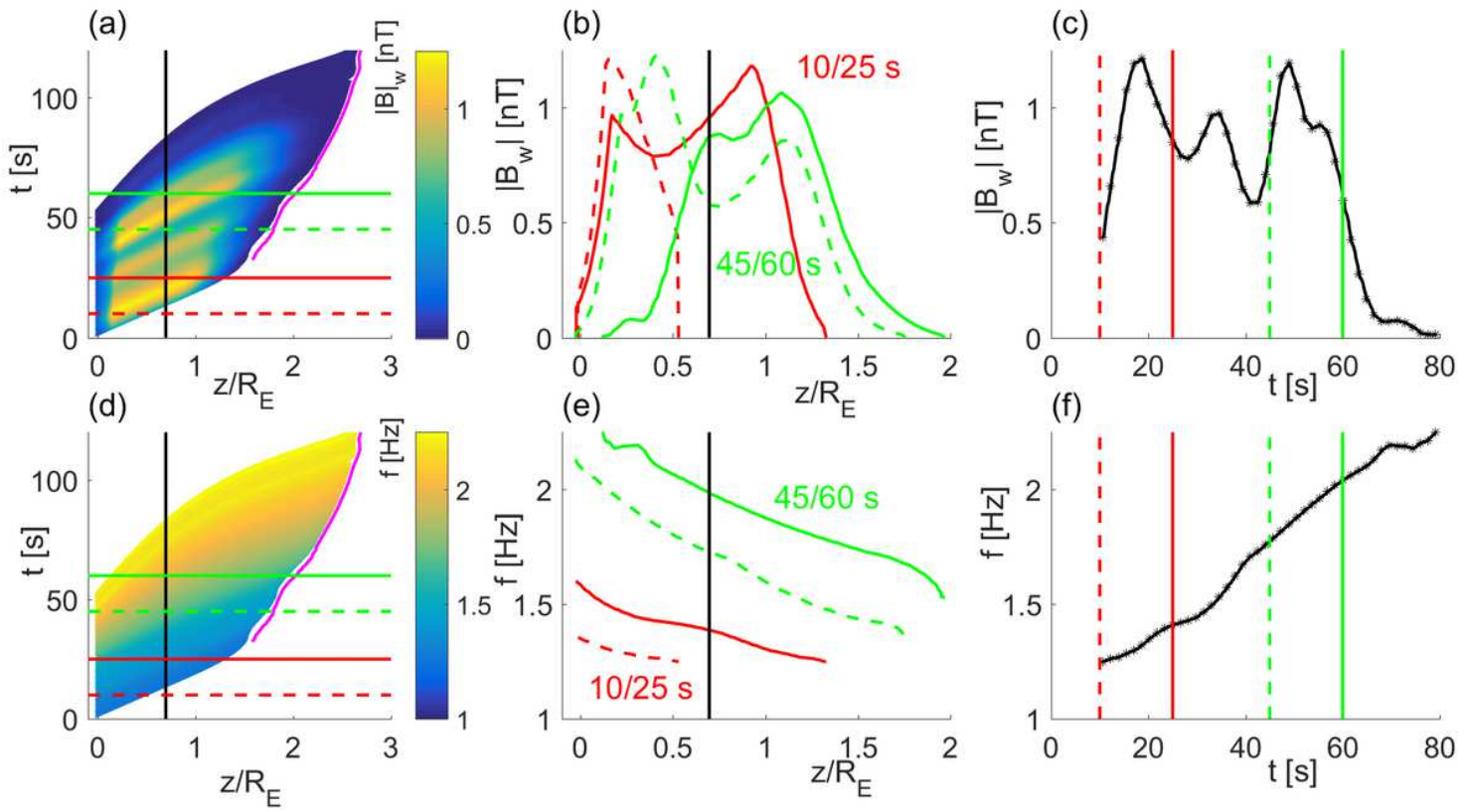


Figure 2

Please see the Manuscript PDF file for the complete figure caption

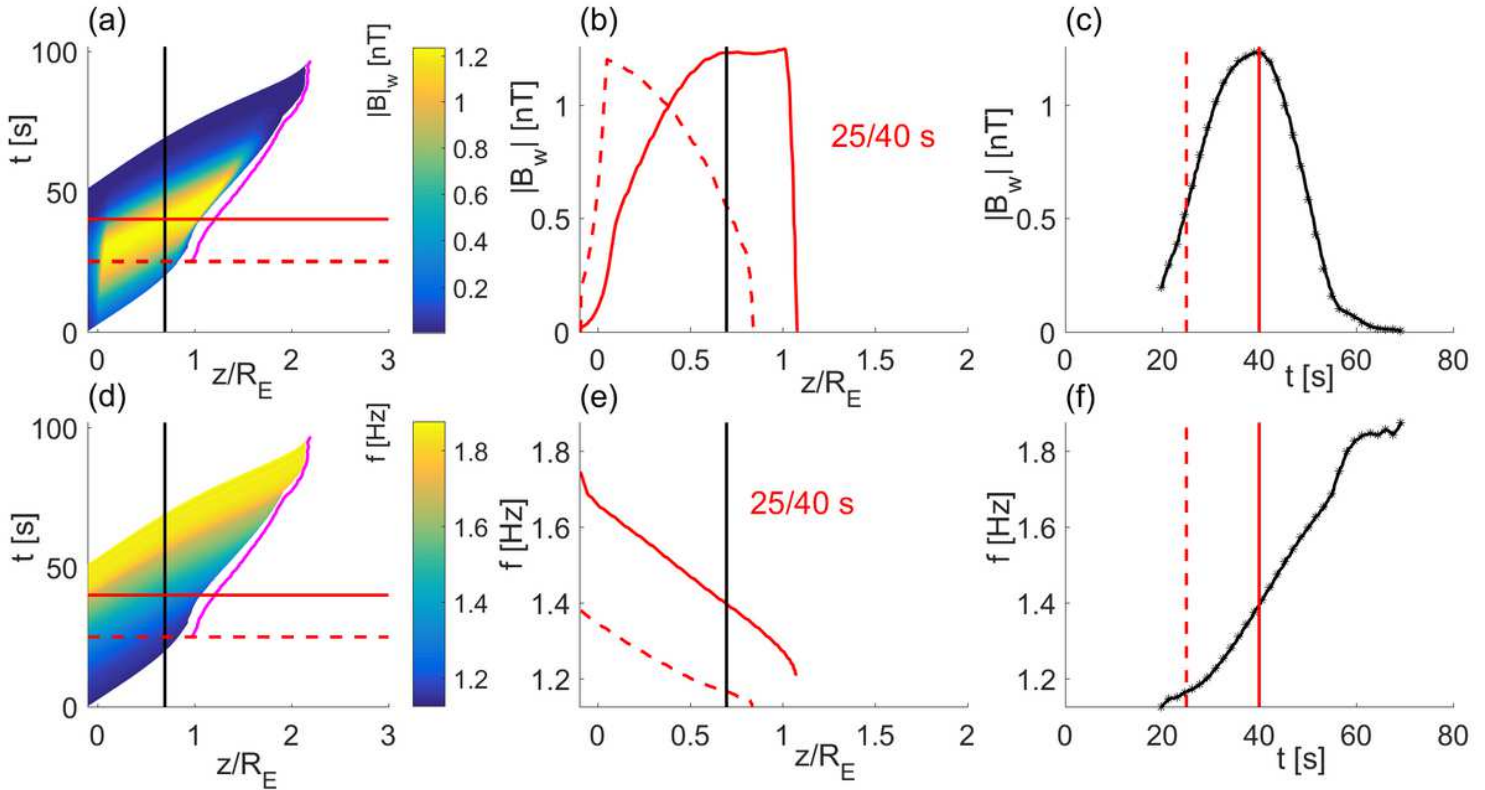


Figure 3

Please see the Manuscript PDF file for the complete figure caption

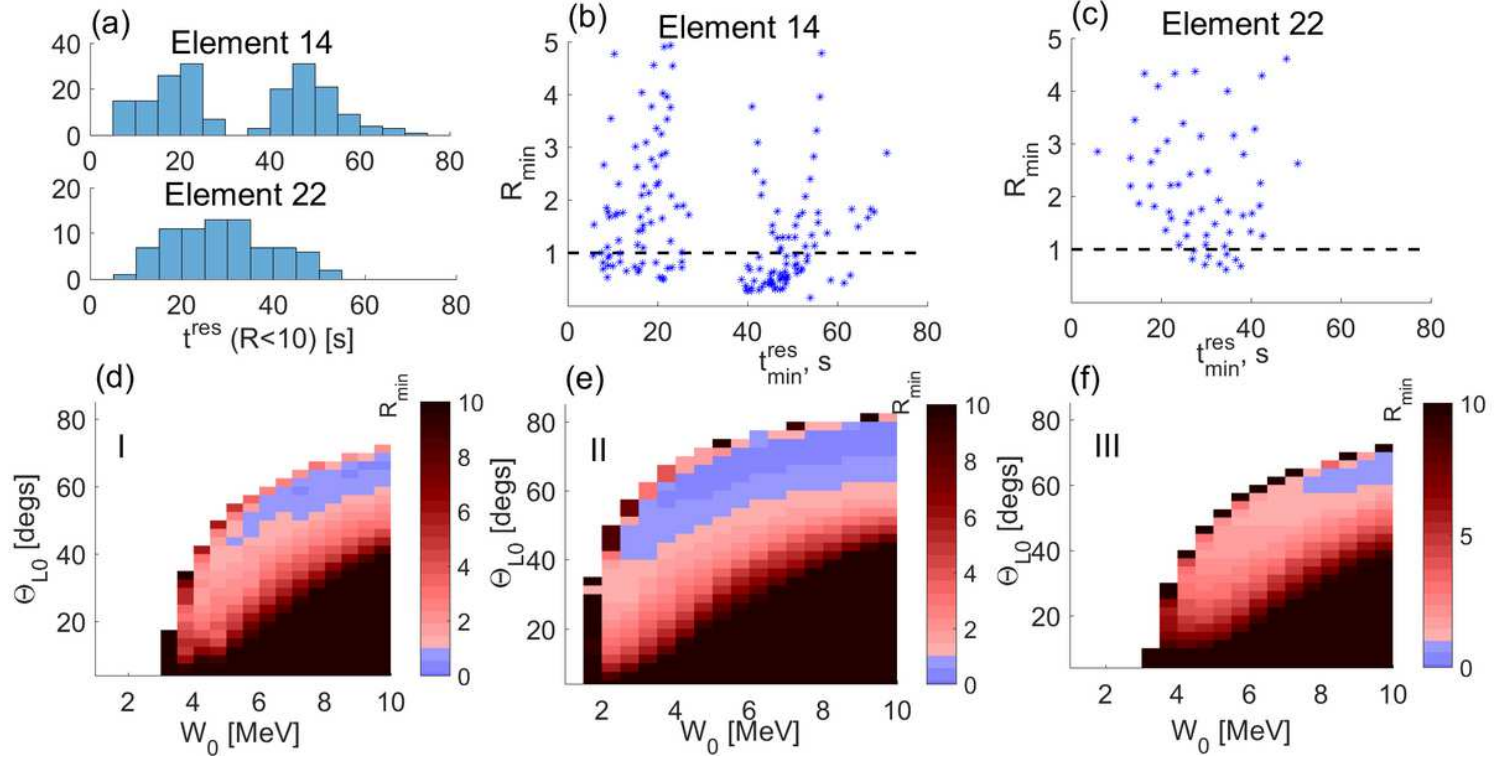


Figure 4

Please see the Manuscript PDF file for the complete figure caption

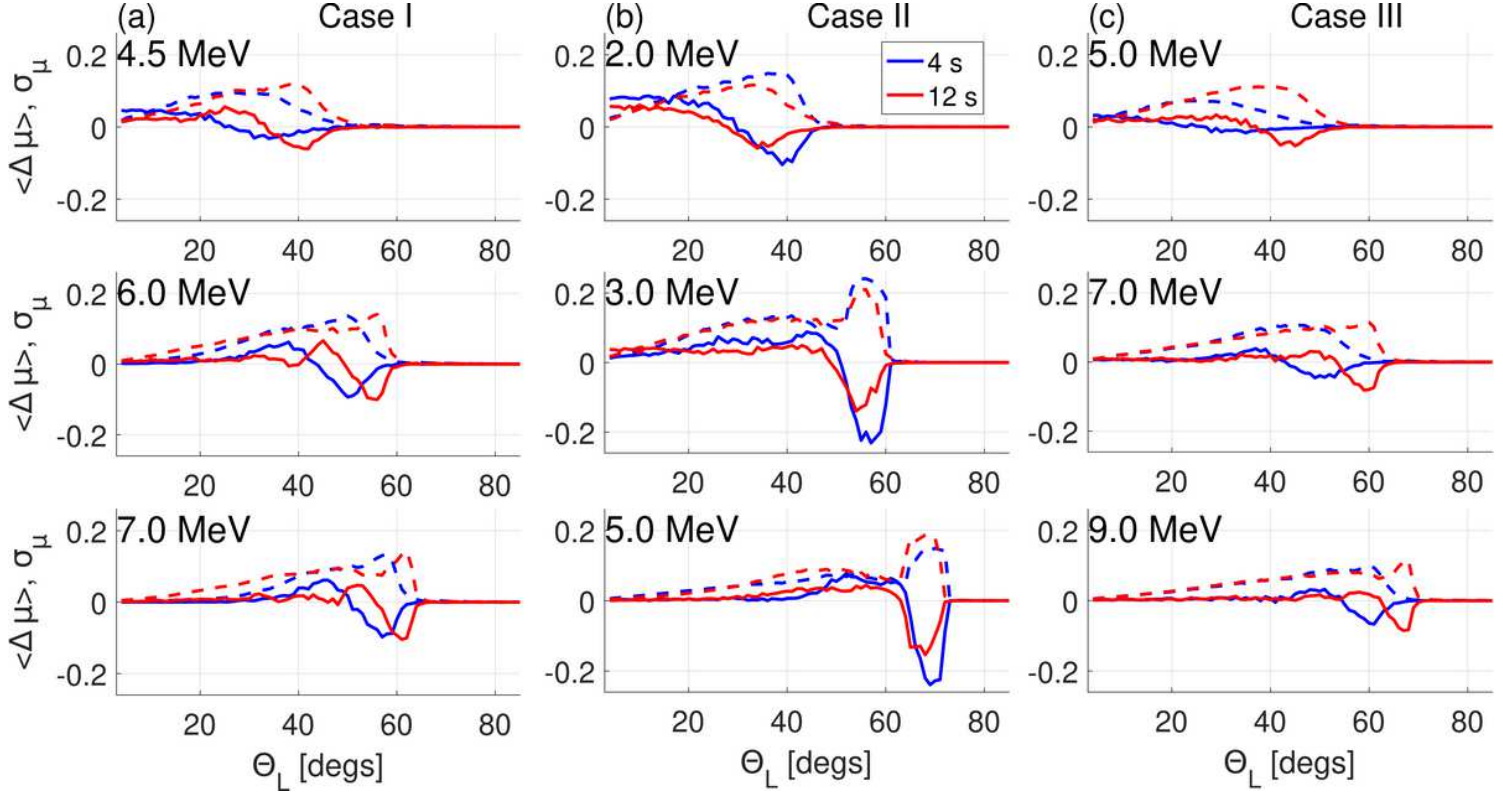


Figure 5

Please see the Manuscript PDF file for the complete figure caption

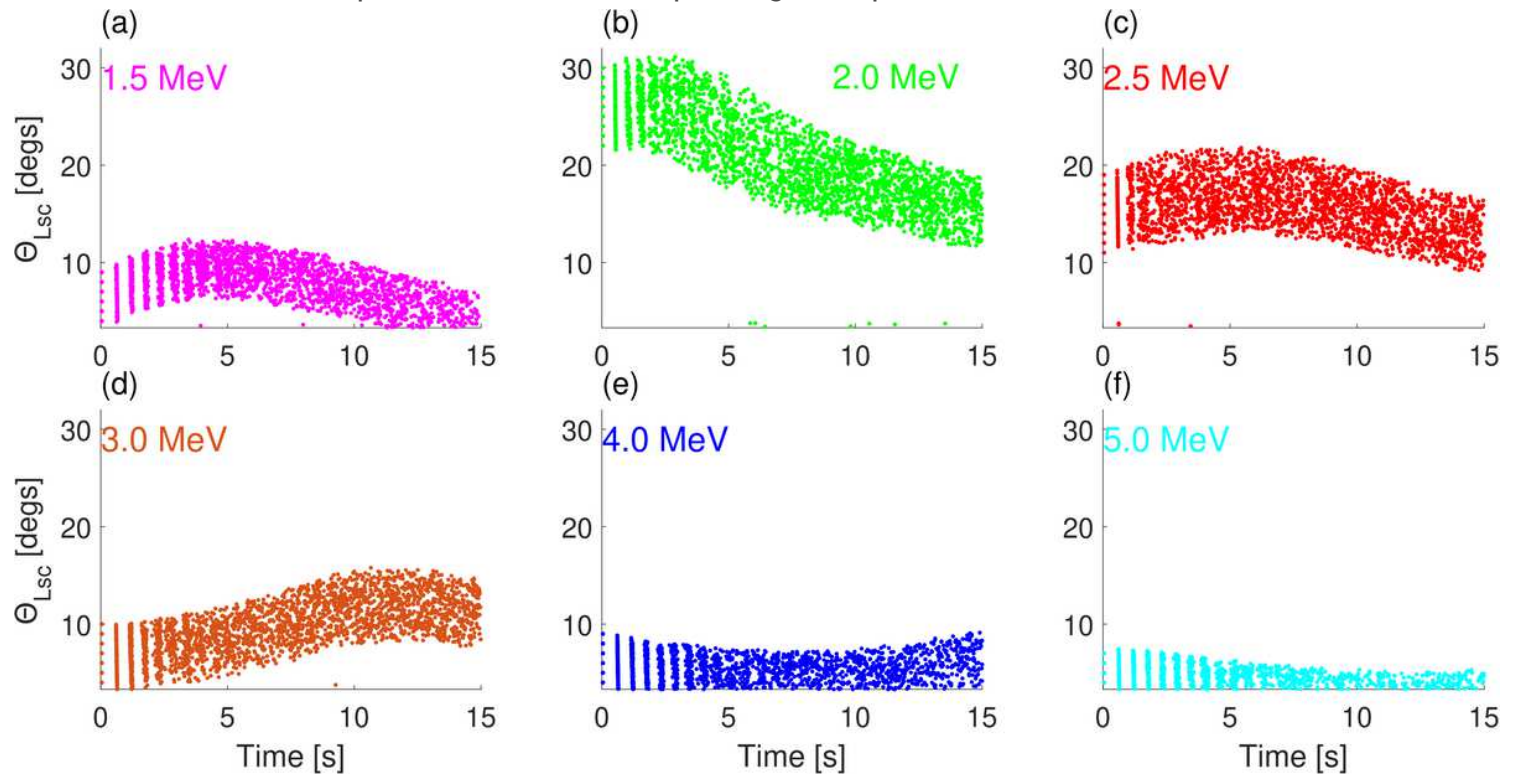


Figure 6

Please see the Manuscript PDF file for the complete figure caption

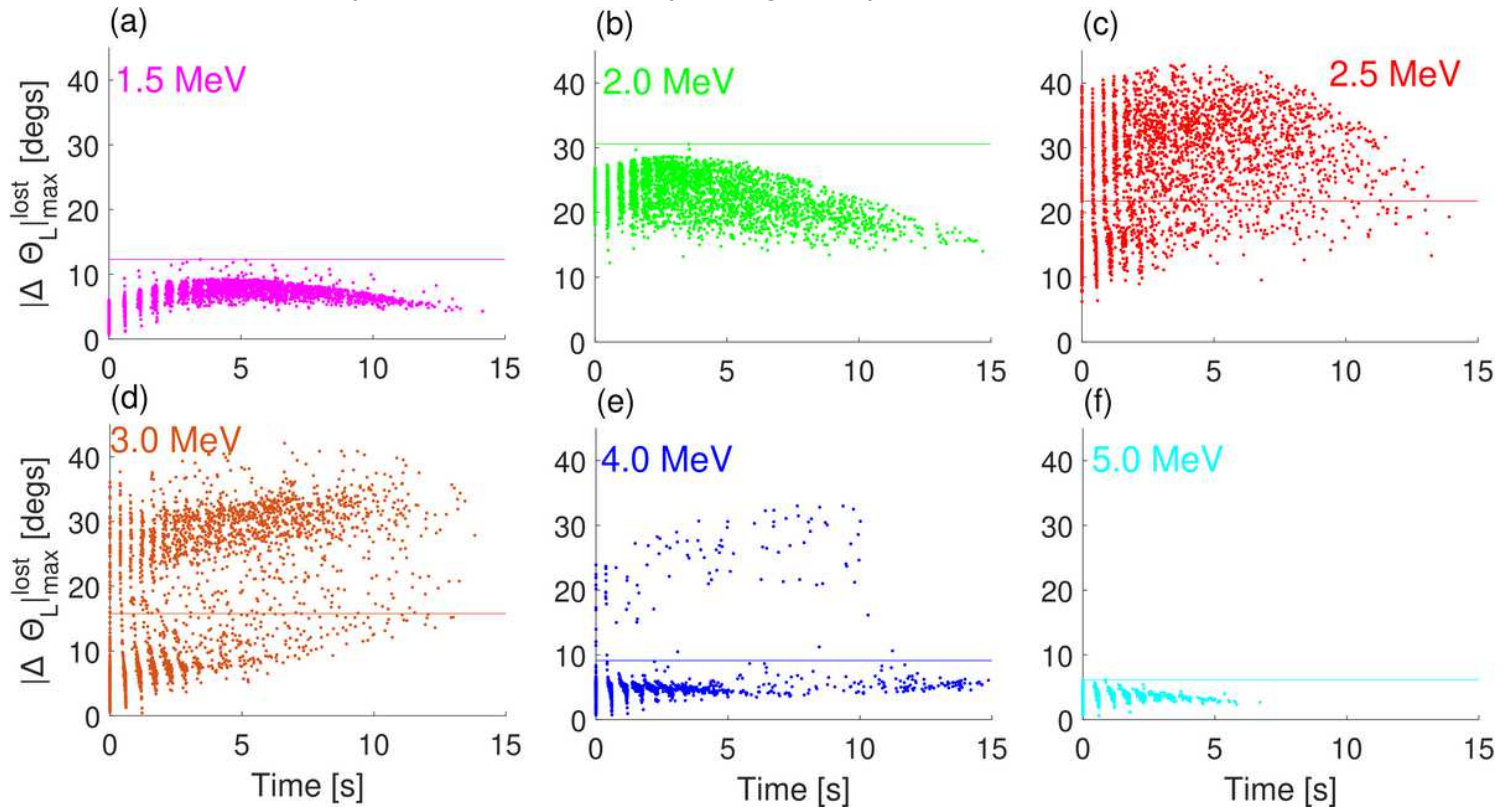


Figure 7

Please see the Manuscript PDF file for the complete figure caption

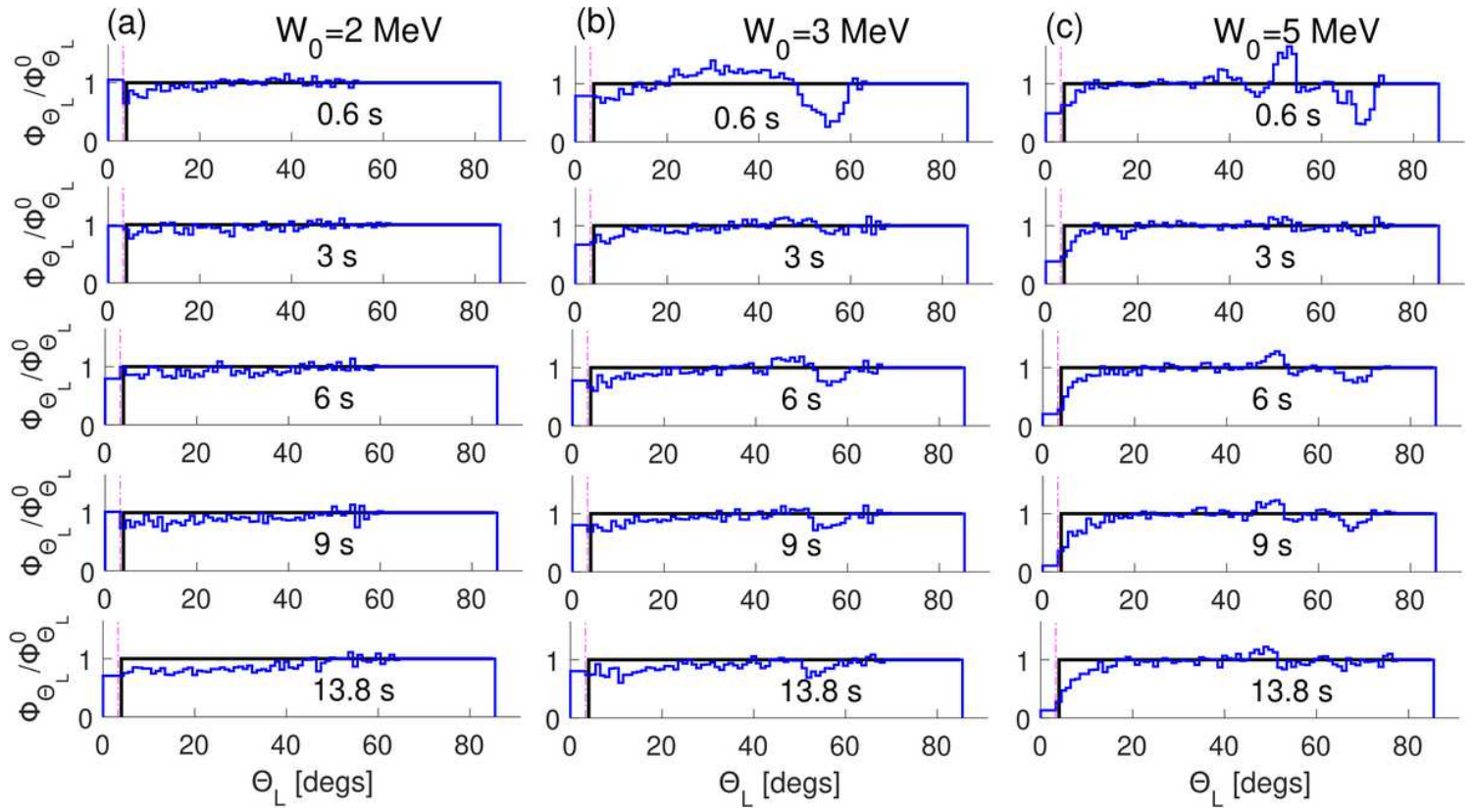


Figure 8

Please see the Manuscript PDF file for the complete figure caption

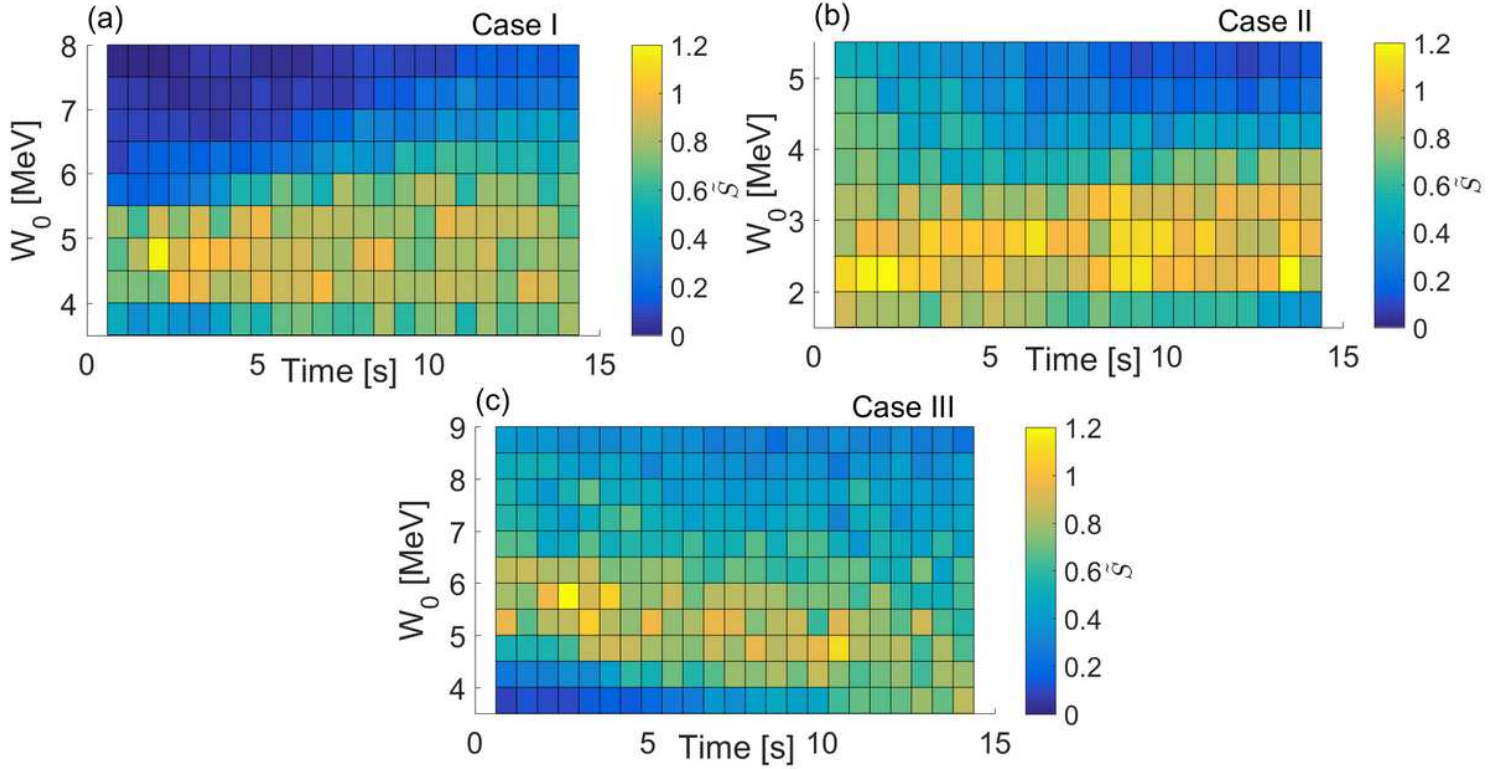


Figure 9

Please see the Manuscript PDF file for the complete figure caption

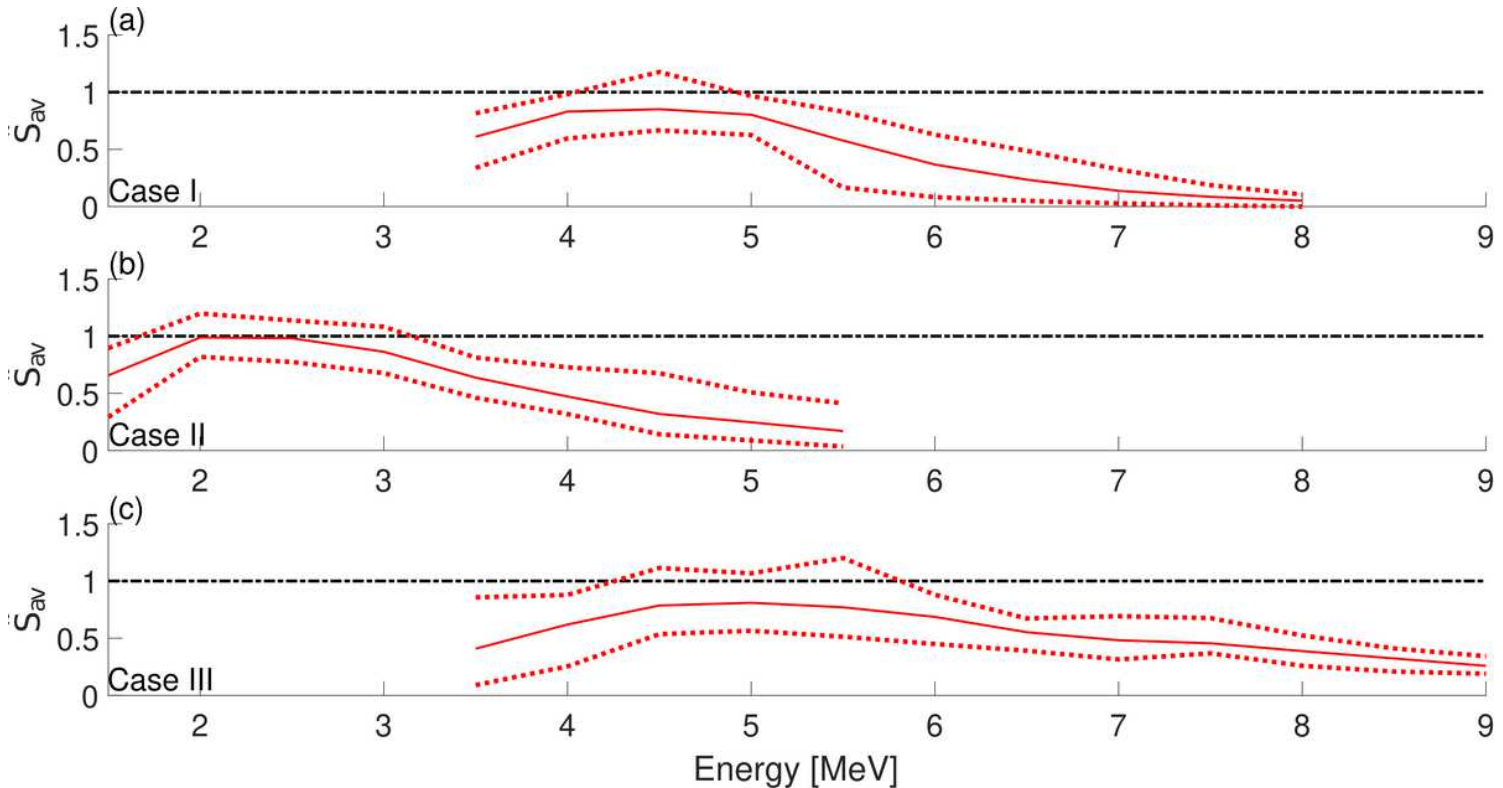


Figure 10

Please see the Manuscript PDF file for the complete figure caption

Supplementary Files

This is a list of supplementary files associated with this preprint. Click to download.

- [GDLGrA.png](#)